

Diurnal variation of tropospheric relative humidity in tropical region

Isaac Moradi^{1,2}, Philip Arkin¹, Ralph Ferraro², Patrick Eriksson³, and Eric Fetzer⁴

¹ESSIC, University of Maryland, College Park, Maryland, USA.

²STAR, NOAA, College Park, Maryland, USA.

³Chalmers University of Technology, Gothenburg, Sweden.

⁴Jet Propulsion Laboratory (JPL), CalTech, California, USA.

Correspondence to: Corresponding author: Isaac Moradi, ESSIC, University of Maryland, College Park, MD 20740, USA. (imoradi@umd.edu)

Abstract. Despite the importance of water vapor especially in the tropical region, the diurnal variations of water vapor have not been completely investigated in the past due to the lack of adequate observations. Measurements from Sondeur Atmosphérique du Profil d'Humidité Intertropicale par Radiométrie (SAPHIR) onboard the low inclination Megha-Tropiques satellite with frequent daily
5 revisits provide a valuable dataset for investigating the diurnal and spatial variation of tropospheric relative humidity in the tropical region. In this study, we first transformed SAPHIR observations into layer-averaged relative humidity, then partitioned the data based on local observation time into 24 bins with a grid resolution of one degree. Afterwards, we fit the Fourier series to the binned data. Finally, the mean, amplitude, and diurnal peak time of relative humidity in tropical region were calculated for each grid point using either the measurements or the Fourier series. The results were
10 separately investigated for different SAPHIR channels as well as for relative humidity with respect to both liquid and ice phases. The results showed that the wet regions are normally associated with convective regions, and the dry regions with the subsidence regions which is consistent with the previous studies. The new analysis reveals new findings for the diurnal amplitude and peak time of
15 tropospheric relative humidity. The results showed a large inhomogeneity in diurnal variation of tropospheric relative humidity in tropical region. Although, the peak of RH generally occurs over night or in early morning, there are several regions where the diurnal peak occurs at other times of the day. The results showed that the diurnal amplitude is less than 10 % in middle and upper troposphere, but it is up to 30 % in lower troposphere over land.

20 1 Introduction

Water vapor is the dominant natural greenhouse gas in the atmosphere, thus it significantly influences the Earth's climate and energy budget. Water vapor is responsible for nearly half of the poleward and most of the upward heat transfer, and also affects the Earth's hydrologic cycle through evaporation

and condensation (Sherwood et al., 2010). In addition, water vapor drives extreme weathers such
25 as rainstorm, floods, and the initiation of convective cyclones (Keil et al., 2008). Water vapor in
the free troposphere, the layer expanding from 1-2 km above the surface up to tropopause, strongly
contributes to the water vapor feedback through radiative processes (Held and Soden, 2006; Tren-
berth et al., 2009; Dessler and Sherwood, 2009), with maximum feedback occurring in the tropical
free troposphere (Dessler et al., 2008). Therefore, water vapor is expected to also play an important
30 role in global warming and climate change predictions (Cess et al., 1990). For instance, assuming
a constant relative humidity (RH) in climate models doubles the rise in temperature compared to
when the water vapor feedback is forced to be zero (Minschwaner and Dessler, 2004; Soden et al.,
2005). Additionally, the net cooling of the atmosphere is indirectly affected by tropospheric wa-
ter vapor through the initiation of clouds and convective heating (Sherwood, 2010). Diurnal cycles
35 in temperature and moisture drive diurnal variations in temperature, precipitation, and convective
activities (Chung et al., 2007), therefore, are expected to interact significantly with, for example,
changes in global mean humidity or temperature. However, current climate and numerical weather
prediction models do not adequately simulate the diurnal variation of tropospheric humidity (Chung
et al., 2013), a failing that is very likely to lead to inaccuracies in their simulations. As models are
40 improved, accurate observations of diurnal cycles of humidity will be crucial in verifying the validity
of simulations.

Most studies in the past have mainly used infrared (IR) satellite data from geostationary orbits to
evaluate the diurnal cycle of RH (e.g., Soden, 2000; Tian, 2004; Chung et al., 2007). Chung et al.
(2013) evaluated the diurnal variation of UTH in reanalysis using Meteosat-5 data and reported a
45 distinct diurnal cycle of UTH over tropical convective regions. Schröder et al. (2014) developed
a homogenized dataset for free tropospheric humidity under clear sky conditions. Although, this
dataset is valuable in clear-sky conditions especially over land, however its is biased towards dry
conditions in the tropical region as most of the IR measurements are filtered out over the subsidence
regions because of the presence of deep-convective clouds. Chung et al. (2007) evaluated the diurnal
50 variation of RH over Africa using IR observations. They reported a large diurnal amplitude over
land but a smaller amplitude over oceanic subsidence regions. In an early attempt to relate spatial
distribution of tropospheric humidity with physical mechanisms, Udelhofen and Hartmann (1995)
evaluated the decrease in relative humidity with distance from the edge of the clouds. They reported
that the rate of decrease in UTH is lower in Intertropical Convergence Zone (ITCZ) than in the
55 subsidence regions showing a wider impact for the ITCZ clouds on the environment surrounding the
clouds. It should be noted that IR observations are very sensitive to clouds, thus the data need to be
strictly filtered for clouds before being analyzed. The cloud screening removes a large portion of the
IR measurements especially over convective regions. The rejected observations normally represent
moist conditions, therefore the IR results only represent dry conditions. For instance, John et al.
60 (2011) indicated that the IR cloud screening introduces on average around 10 % systematic error

in the upper tropospheric humidity values. It is clearly shown in John et al. (2011) that the cloud screening especially removes most of the data over the convective regions causing a large systematic bias in the RH analysis for the convective regions. It should be noted that among the channels, the upper tropospheric channels are less sensitive to clouds than the lower channels, because the weighting functions for the upper channels normally peak above the clouds, therefore it is expected that the dry bias due to cloud screening is even larger for the middle and lower tropospheric channels. It should be noted that the cloud screening not only impacts the RH amplitude by removing the moist conditions, but it also impacts the diurnal peak time. Thus, the analyses performed using IR observations are biased for both the spatial distribution and the diurnal cycle of the RH values.

One exception is Kottayil et al. (2013) that used multi-instrument microwave measurements from five polar-orbiting satellites to investigate the diurnal variation of brightness temperature (Tb) over the globe. However, other issues are involved when data from polar-orbiting instruments are utilized. First, polar-orbiting satellites only overpass each location twice a day, thus even a constellation of five satellites do not properly represent the diurnal variation of RH (e.g. see Figure 1 in Kottayil et al. (2013) for the temporal coverage in different years). The orbital drift only slightly enhances the temporal coverage of the data. Second, the multi-instrument differences are an important issue when data are combined. Kottayil et al. (2013) used a dataset that was inter-calibrated using Simultaneous Nadir Observations (SNO). The inter-satellite differences are normally scene dependent, however SNO's normally happen in the polar region so cannot sufficiently resolve the scene dependency due to non-linearity in the calibration of microwave instruments. The observations discussed above are all downward looking, covering altitudes up to about 300 hPa. Diurnal RH variations at higher altitudes have been studied by microwave limb sounding data. Coarse estimates, having a resolution of 6-hour in local time, were provided by Eriksson et al. (2010), by combining data from two different sun-synchronous satellites, Aura Microwave Limb Sounder (MLS) and Odin Sub-Millimeter Radiometer (SMR). These estimates were compared to some climate models and it was found that the models tend to underestimate diurnal variations and partly also simulate maximum RH at wrong local time. Later, Eriksson et al. (2014) derived diurnal variations using the Superconducting Submillimeter-Wave Limb-Emission Sounder (SMILES) instrument. SMILES measurements are only available for a 6-month period, but the measurements are made at different local times so suitable for evaluating the diurnal variation. The SMILES data were found to confirm the main features reported by Eriksson et al. (2010).

In summary, despite the importance of water vapor and its distribution in time and space, there still exists a considerable uncertainty in our knowledge of the diurnal and spatial distribution of tropospheric water vapor. The efforts so far have not been able to clearly determine the temporal and spatial distribution of water vapor in the atmosphere due to the lack of adequate observations. This study benefits from observations from Sondeur Atmosphérique du Profil d'Humidité Intertropicale par Radiométrie (SAPHIR) onboard Megha-Tropiques (M-T), a low-inclination satellite with fre-

quent revisits in tropical region between 35 °N and 35 °S. SAPHIR is equipped with six water vapor channels sensitive to upper to lower tropospheric RH. SAPHIR provides a great opportunity to analyze the diurnal and spatial variation of RH in the tropical region using data from a single instrument (Moradi et al., 2015b). As stated before, relative humidity is the ratio of water vapor pressure to the saturated vapor pressure. The water vapor pressure depends mainly on the water vapor content of the atmosphere, but the saturated vapor pressure depends on the air temperature. Therefore, the diurnal variation of RH does not necessary indicate change in the water vapor content of the atmosphere, because it is affected by both diurnal variation of water vapor and air temperature. For instance, change in the amount of lower tropospheric water vapor over deserts is very small during day, but RH can significantly change because of change in air temperature. Therefore, it is more desired to analyze the diurnal variation of absolute humidity parameters. However, measurements from microwave water vapor channels are most sensitive to change in RH and cannot be used to derive absolute humidity parameters. The rest of the paper is organized as follows: Section 2 discusses satellite data used in this study, Section 3 presents the methodology including the satellite Tb to RH transformation method as well as Fourier series, Section 4 discusses the results, and Section 5 summarizes the study.

2 Satellite Data

Megha-Tropiques is a low-inclination satellite launched in November 2011 that frequently visits the tropical band between 35 °S and 35 °N. SAPHIR is a microwave humidity sounder onboard the M-T satellite that measures tropospheric RH using six channels centered around the water vapor absorption line at 183 GHz. All SAPHIR channels have double pass-band with horizontal polarization operating at 183 ± 0.20 , 183 ± 1.10 , 183 ± 2.80 , 183 ± 4.20 , 183 ± 6.80 , and 183 ± 11.0 GHz. The instrument swath width is 1700 km, and the resolution is 10 km at nadir for all the channels. Figure 1 shows the weighting functions for the SAPHIR channels which are roughly sensitive to upper (channel 1 peaking around 10 km) to lower troposphere (channel 6 peaking around 2 km). It should be noted that one limitation of the measurements from microwave (as well as infrared) humidity sounders is that the peak of Jacobians changes with the water vapor content of the atmosphere. For instance shaded regions in Figure 1 depict the range of Jacobinas for SAPHIR channels derived from the European Organization for the Exploitation of Meteorological Satellites (EUMETSAT) database (Chevallier et al., 2006). However, this shift is expected to be small in tropical region and should not affect the results. We used SAPHIR L1A data, for the period January 2012 to September 2015, processed by the Centre National d'Etudes Spatiales (CNES).

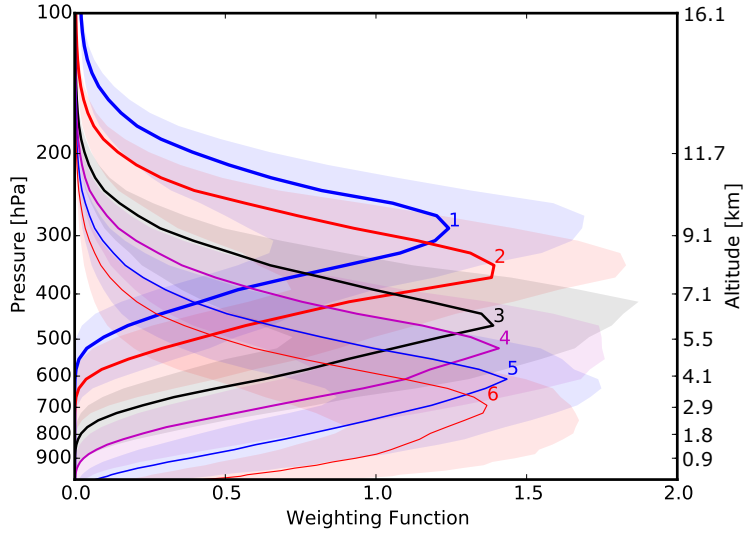


Figure 1. The weighting functions for the SAPHIR channels calculated using a subset of EUMETSAT profiles. The selected subset includes 5000 profiles, so that the shaded areas show the range for 25th and 75th percentiles of all profiles. The solid lines show the 50th percentile and the channels' numbers are printed on the plot.

130 3 Methodology

This section discusses the methodology that is used to transform satellite radiances into RH and also Fourier series that are used to investigate the diurnal cycle of tropospheric RH.

3.1 Satellite Tb to RH Transformation

A simple method that was developed by Soden and Bretherton (1993) has been widely used in the past to convert satellite microwave measurements to layer averaged RH (e.g., Buehler and John, 2005; Moradi et al., 2010, 2015a). In this simple relation, the satellite Tb's are linearly related to the natural logarithm of layer averaged humidity as follows:

$$\ln(RH^{ch}) = a^{ch} + b^{ch} \times Tb^{ch} \quad (1)$$

where a and b are empirical coefficients that change with the earth incidence angle unless the satellite Tb's are corrected for the limb-effect, and the ch stands for the channels. Since calculating the empirical coefficients as a function of earth incidence angle introduces a very large look-up table; similar to Moradi et al. (2015a), we first applied a limb-correction technique to SAPHIR Tb's then used the same empirical coefficients for all the incidence angles. We calculated the limb-darkening (ΔTb) as the difference between Tb for each beam position and corresponding nadir Tb using data averaged over a long-period of time:

$$Tb^n = Tb(\theta) - \Delta Tb$$

$$\Delta Tb = c \times \ln(\cos\theta) \tag{2}$$

where Tb^n is Tb at sub-nadir footprint, and $Tb(\theta)$ is Tb at any given θ (Moradi et al., 2015a). Since the SAPHIR data do not suffer from scan asymmetry, we preferably used the satellite data to develop the limb-correction technique. As shown in Figure 2, the limb-darkening is stronger for the channels operating near the center of the water vapor absorption line than channels operating near the wings of the line. Figure 2 also shows the values for the coefficient c in Equation 2 for different SAPHIR water vapor channels.

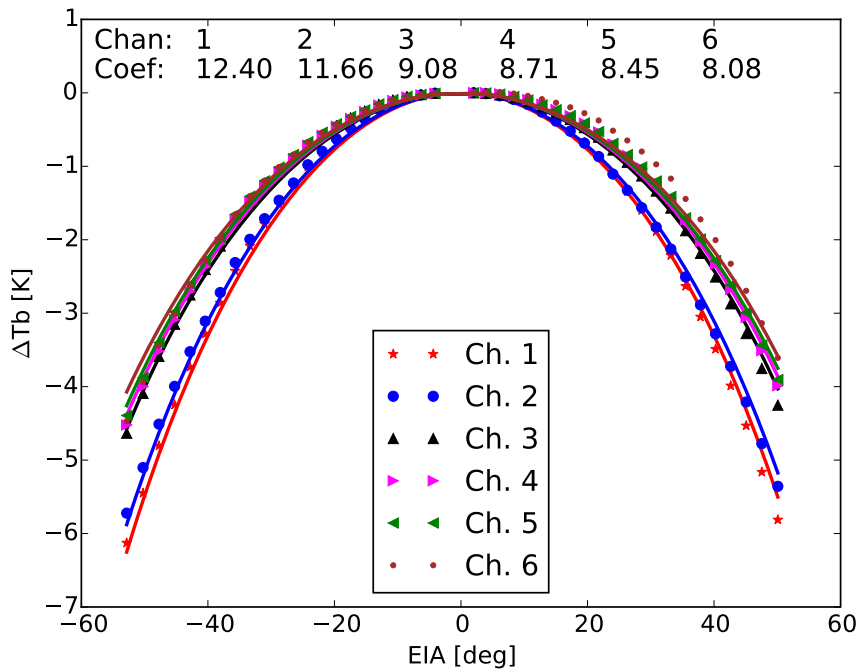


Figure 2. Limb-darkening effect as a function of EIA for different SAPHIR channels. The empirical coefficient for Equation 2 are also printed on the plot.

Microwave satellite data are less sensitive to clouds than IR data, however microwave measurements may also be affected by optically thick clouds. Since the empirical coefficients are only valid for clear-sky radiances, the data affected by clouds should be excluded from the analysis. We used the same thresholds proposed by Moradi et al. (2015b) to screen-out the clouds using the differences between Tb's of an upper channel (Tb2, channel 2 operating at 183 ± 1.10 GHz) and a lower channel (Tb5, channel 5 operating at 183 ± 6.8 GHz). The satellites Tb's are cloud free if $Tb2 - Tb5 < -15$ K and $Tb2 > 240$ K. More details are provided in Moradi et al. (2015b).

In addition to clouds, some of the satellite radiances may be affected by the surface emissivity which results in high (low) Tb values over land (ocean). Because of the inverse relation between the

RH and TB, this corresponds to artificially low (high) RH values over land (ocean) for the measurements that are affected by the surface. We used a threshold for Tb's to exclude the measurements that are affected by the surface. Because the emissivity in microwave frequencies is low over ocean (0.5-0.7) and high over land (about 0.9), the Tb's affected by the surface are normally high over land and low over ocean. We used a subset of Atmospheric Radiation Measurement Program (ARM) radiosonde data and also radiative transfer calculations to determine the thresholds for Tb's that are affected by either land or ocean. We performed two set of radiative transfer calculations using the same radiosonde profiles but different emissivity values for land and ocean. Figure 3 shows the Tb's histograms for different SAPHIR channels, when the difference between simulated Tb's for land and ocean is less than 0.01 K. Therefore, the histograms show the range of Tb's that are not affected by the surface. Based on these histograms we defined the following thresholds for excluding surface affected observations from analysis for channels 1-6, respectively: 230 K to 270 K, 240 K to 280 K, 250 K to 290 K, 255 K to 295 K, 265 K to 295 K, and 270 K to 300 K. The lowest threshold is applied when the observations are affected by the sea surface and the maximum applies when the observations are affected by the land surface. No filter is applied for topography, thus the results over mountainous terrains should be considered with caution since the satellite radiances are averaged over a spatially very inhomogeneous region.

3.2 Analyzing Diurnal Variation

Fourier series are traditionally used to model the diurnal cycle of meteorological variables such as temperature and humidity. Fourier series are periodic functions expressed in terms of sine and cosine functions as follows:

$$F(x) = a_0 + \sum_{k=1}^K [a_k \cos(kx) + b_k \sin(kx)] \quad (3)$$

where x represents time of the day in radians ($x \in [-\pi, \pi]$) and can be calculated as $x = \frac{t-t_1}{t_1}\pi$, where t_1 is equal to 12, t is time of the day in hour, and a_0 , a_k , and b_k are the Fourier coefficients that can be calculated using the following relations:

$$\begin{aligned} a_0 &= \frac{1}{\sum w_i} \sum w_i y_i \\ a_k &= \frac{2}{\sum w_i} \sum w_i y_i \cos(kx_i) \\ b_k &= \frac{2}{\sum w_i} \sum w_i y_i \sin(kx_i) \end{aligned} \quad (4)$$

where y_i are the measurements and w_i indicates the weights given to each measurement. The weights are calculated as $\frac{1}{\sigma}$, where σ is the standard deviation of all the measurements within each individual bin. We assume that the data are equally spaced and the points define the middle of

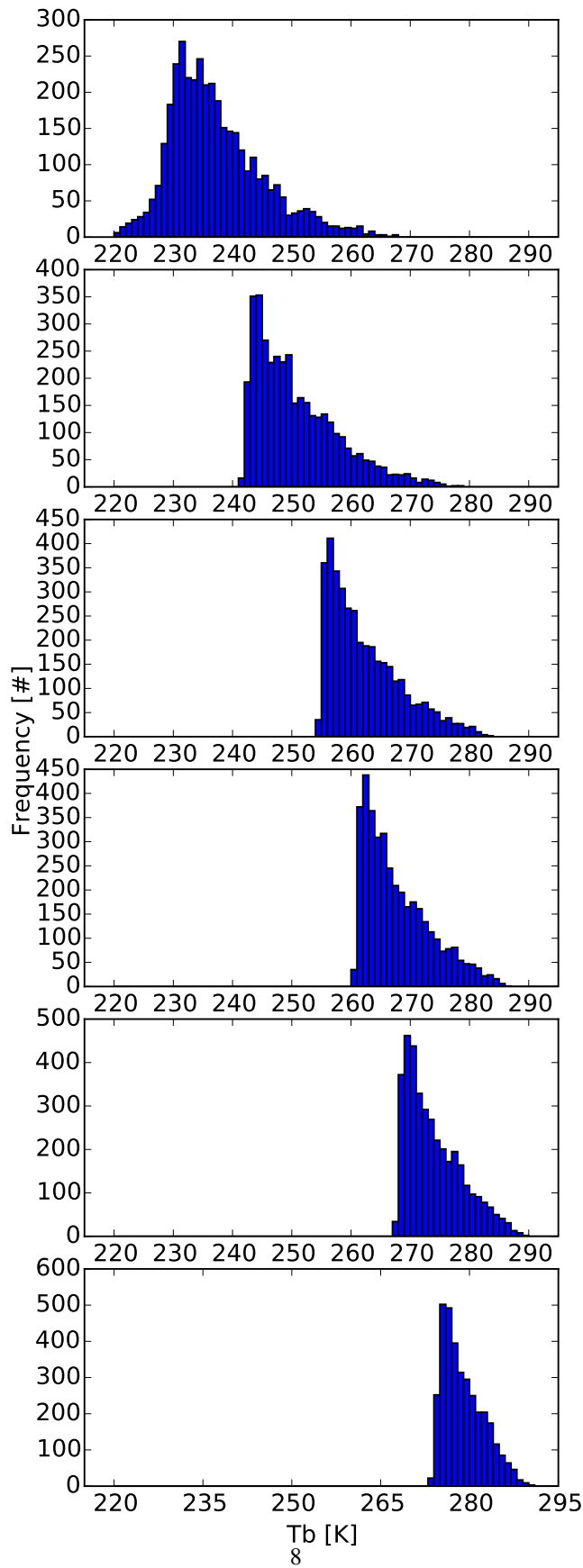


Figure 3. Histograms for the distribution of Tb's that are not affected by the surface. The panels from top to bottom are for SAPHIR channel 1 (upper troposphere) to channel 6 (lower troposphere), respectively.

each interval, so that n data points can be used to divide the space $[-\pi, \pi]$ into n equal intervals
195 so that $\Delta x = \frac{2\pi}{n}$. Some of the previous studies, e.g., Tian (2004) and Kottayil et al. (2013), have
used least square techniques to determine the Fourier coefficients. However, as shown in Equation
4, the coefficients can be mathematically and directly calculated from the measurements. It is also
required to determine number of terms that Fourier series should be expanded (i.e., K in Equation
3). However, there is no standard method to determine this number. We evaluated the mean absolute
200 difference between the measurements and the values calculated using Fourier series to determine
number of terms that Equation 3 needed to be expanded (see Section 4.4 for more information). It
was found out that one term is sufficient over regions with small diurnal variation, but the series
needed to be expanded two terms to properly cover the diurnal variation over regions with a larger
diurnal amplitude.

205 4 Results

4.1 Tb to RH Transformation

We used a subset of the ARM radiosonde data to calculate the empirical coefficients (a and b) for
Equation 1. Since the saturated vapor pressure can be calculated with respect to either liquid (tem-
peratures above the freezing point of water) or ice phase (temperatures below the freezing point of
210 water), the empirical coefficients can be defined the same way with respect to saturated vapor pres-
sure over either liquid or ice. We use RH_I to refer to RH with respect to ice and RH_L for RH over
liquid. It is expected that at least in the middle and upper troposphere (channels 1-4), the air temper-
ature is generally below the freezing point thus we need to use the saturated vapor pressure over ice.
Additionally, for the lower channels (channels 5 and 6) the saturated vapor pressure expressions for
215 ice and liquid approach each other. Therefore, in most cases we only present the results for the ice
phase (RH_I) and the results for the liquid phase (RH_L) are provided in supplementary materials.

Figure 4 shows an example of the relation between satellite Tb's and natural logarithm of layer
averaged RH_I for SAPHIR channel 2. Channel 2 of SAPHIR operates at 183 ± 1 GHz which is
similar to a channel on many humidity sounders such as Advanced Technology Microwave Sounder
220 (ATMS), AMSU-B, and MHS. Therefore, the results can be directly compared with the previous
studies. For instance, the coefficients shown in Figure 4 are consistent with Buehler and John (2005),
Moradi et al. (2010), and Moradi et al. (2015a).

The empirical coefficients for all the channels are presented in Table 1 with respect to both liquid
and ice. Coefficient a for Channel 1 over both ice and liquid is smaller than the same coefficient for
225 other channels, but all other coefficients are very close for all the channels. Both a and b coefficients
are greater over ice than over liquid.

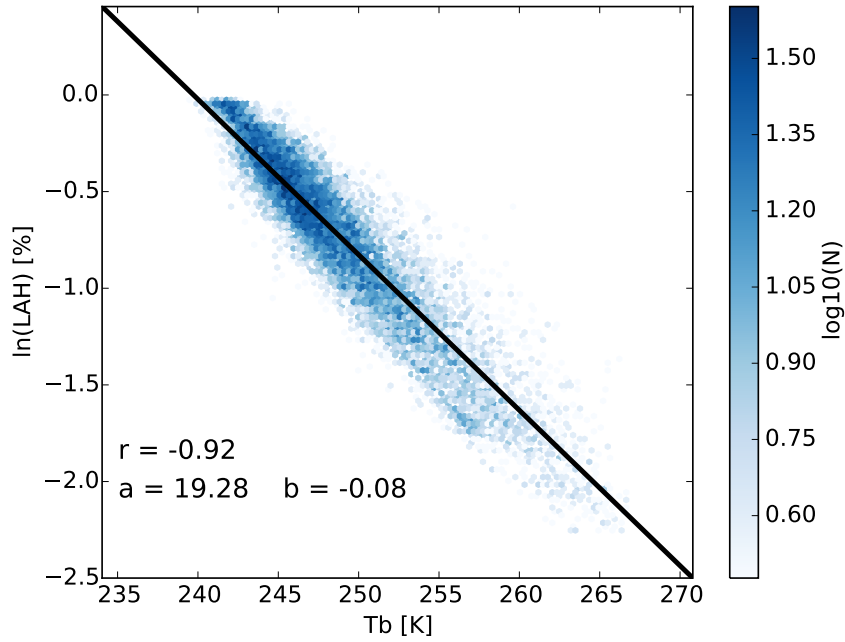


Figure 4. Relation between satellite Tb and natural logarithm of layer-averaged RH_L . The colorbar shows the logarithm of the number of observations.

Table 1. The empirical coefficients for the Tb to RH transformation method for SAPHIR channels.

Chan.	liquid		ice	
	b	a	b	a
1	-0.059621	13.065021	-0.067173	15.231791
2	-0.072363	16.974748	-0.080434	19.281791
3	-0.063765	15.758799	-0.071711	18.022020
4	-0.061421	15.623266	-0.069159	17.818025
5	-0.060818	16.033315	-0.069916	18.581239
6	-0.061955	16.826082	-0.072675	19.818404

4.2 Spatial Distribution of RH

SAPHIR observations are available for the tropical region expanding from about 35 S to 35 N. However, we limited the study to the region between 25 S to 25 N, because the frequency of the revisits is limited outside this region. We first binned the data based on local observation time into a grid of 1.0×1.0 degree. The data-points within each grid-box were gridded into 24 bins based on local observation time. The local time was calculated using Coordinated Universal Time (UTC) and longitude which are both provided in SAPHIR data. Finally, we averaged the data within each grid-box of $1.0^\circ \times 1.0^\circ \times 1.0$ hr. Figure 5 shows average number of observations per hour after the data are filtered for clouds and surface effect. See section 4.3 and Table 2 for details on the boxes shown on the maps. Since the satellite inclination is about 20° , maximum number of observations occurs around 10°N to 20°N and 10°S to 20°S . As shown, on average, 100 to 300 observations are retained for each bin per hour. Over very high elevations the weighting functions for all the channels peak very close to the surface, therefore, the minimum number of observations occurs over mountains such as the Andes in South America.

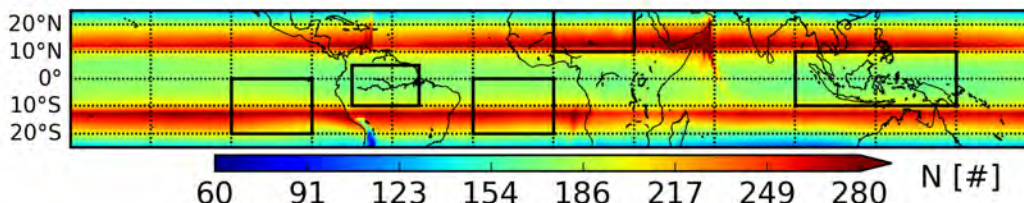


Figure 5. Mean number of overpasses per hour for SAPHIR channel 6. Colorbar shows number of observations per grid point. Number of overpasses are generally higher for other channels than for channel 6.

Figure 6 shows the mean daily RH_L for different SAPHIR channels. As expected, RH significantly changes from upper troposphere (14 % to 36 %) to lower troposphere (41 % to 85 % for Channel 6). Note that in order to avoid the outliers especially over the Andes, in most cases, the upper limits printed on the colorbars show the ninety-ninth percentile. The dry regions are observed over subsidence regions, e.g., South Pacific Ocean, South Atlantic Ocean, as well as Arabian Sea, and are consistent with previous studies (e.g., Moradi et al., 2010; Eriksson et al., 2010; Chung et al., 2007). Additionally, several moist regions are observed over convective regions, e.g., South America, Central Africa, and South Asia also known as Maritime Continent which is located within Tropical Warm Pool. The RH generally decreases with distance from the convective regions which is consistent with previous studies. For instance, Udelhofen and Hartmann (1995) reported that the upper tropospheric humidity rapidly decreases with distance from the convective clouds. The pattern does not change from upper to lower troposphere, but generally the decrease in moisture with distance from the convective region, especially over the Maritime Continent, is faster in lower troposphere

than in upper troposphere. It is also evident that moist regions are connected so that water vapor can
255 be transported across the Equatorial region.

Figure 7 shows the layer-averaged tropospheric RH_I . Because the saturated vapor pressure is lower over ice than over liquid, the RH_I values are greater than the RH_L values. So that RH_I ranges between 18 % to 52 % in upper troposphere (compared to 14 % to 36 % for RH_L), and 38 % to 90 % in lower troposphere (compared to 41 % to 85 % for RH_L). Since we excluded the data that are affected by the surface, no difference between land and ocean is observed along the coastlines. The Andes show a large impact on the lower tropospheric RH but a small impact on upper tropospheric RH. The results for regions such as the Andes should be interpreted with cautious because of uncertainty in the measurements over mountainous regions. The fact that the results do not show a significant land/sea contrast shows that the filter for the surface effect properly removes the surface
260 affected observations. The values reported in Figure 6 are about 10 % to 15 % higher than the values reported in Chung et al. (2007). As stated before, this is because the moist regions are removed from the IR observations due to strict cloud screening. This is also consistent with John et al. (2011) who reported about 10 % dry-bias in clear-sky IR observations in the upper troposphere.

Polar orbiting satellites orbit the earth twice a day, thus the daily average of relative humidity
270 estimated from the measurements of these satellites may be biased depending on the crossing time. In order to evaluate the impact of crossing time on the estimated daily averages, we used the observations from only two overpasses being 12 hours apart, similar to ascending and descending orbits of polar-orbiting satellites. We then computed the mean difference of the daily averages calculated using only two overpasses and the daily averages calculated using all the hourly data. Figure 8 shows the results for the measurements from 01:30 (13:30) local time and Figure 9 shows the results for 09:30 (21:30) local time. In fact we collected all the measurement 30 minutes before and after the aforementioned local time. The mid-night/afternoon orbit (01:30/13:30 local time) matches with several satellites including NOAA Joint Polar Satellite System and NASA A-Train, and the early morning/late evening orbit (09:30/21:30 local time) matches with the orbit for the MetOp satellites. As
275 shown, especially for the lower tropospheric channels, the error is generally larger for 01:30/13:30 local time, because as shown later, in tropical region the peak of RH generally happens in early morning over many regions. In both cases, the error is generally less than 2 % RH_I in upper troposphere and slightly increases in middle troposphere. However, in lower troposphere the difference between the two cases is considerable. The error due to eliminating diurnal variation is more than
280 4 % RH_I especially over land for the measurements from 01:30/13:30 local time and overall less than 2 % RH_I for the measurements from 09:30/21:30 local time. These results show that measurements from polar-orbiting satellites can be used to derive the mean tropospheric humidity in the tropical region with a good accuracy. However, polar-orbiting satellites may not provide a good picture of peak time and amplitude, because these parameters show a large spatial inhomogeneity and obvi-

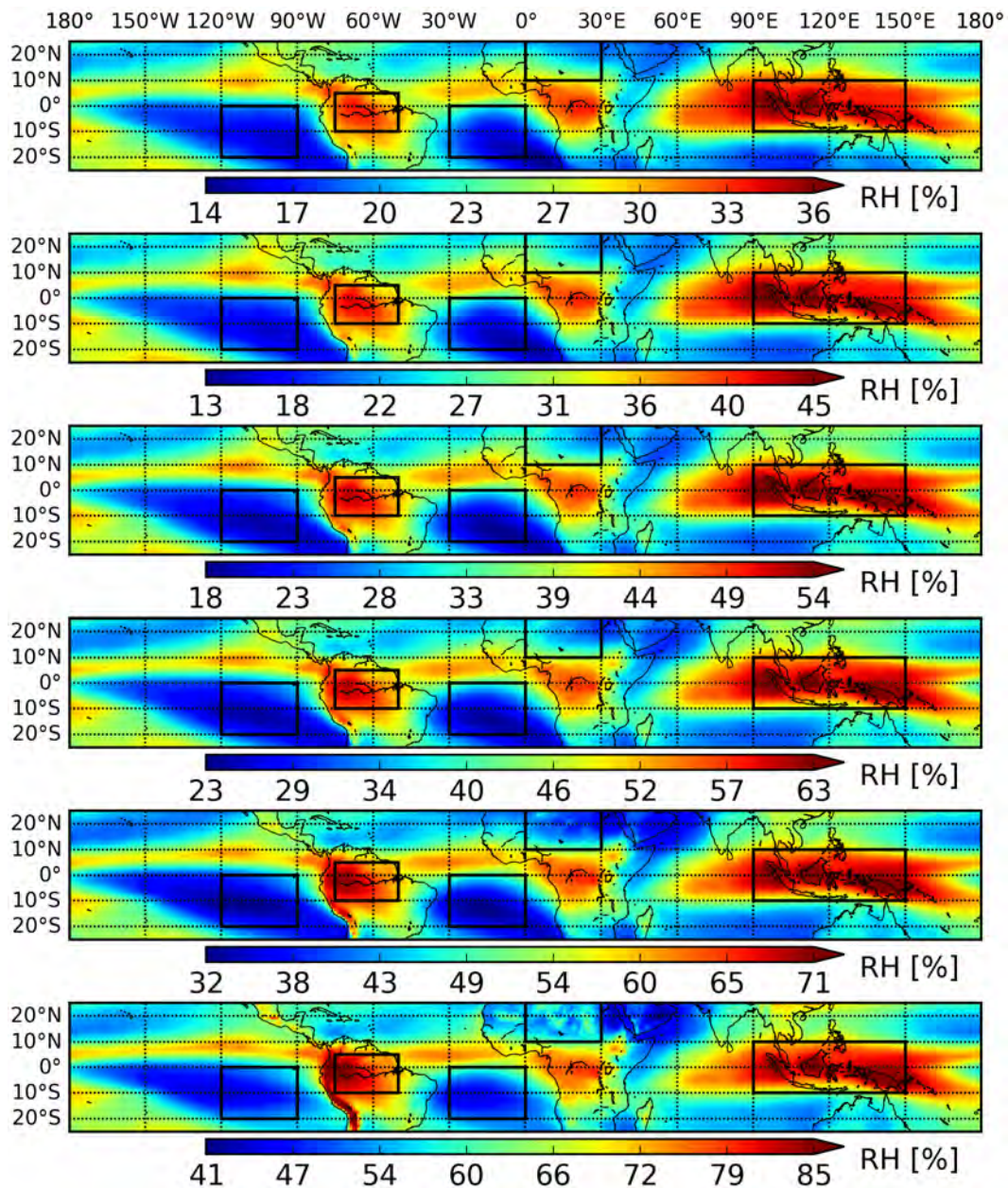


Figure 6. Spatial distribution of layer-averaged RH_L derived using SAPHIR data for the period January 2012 to September 2015. Depicts from top to bottom are for SAPHIR channels 1-6, respectively.

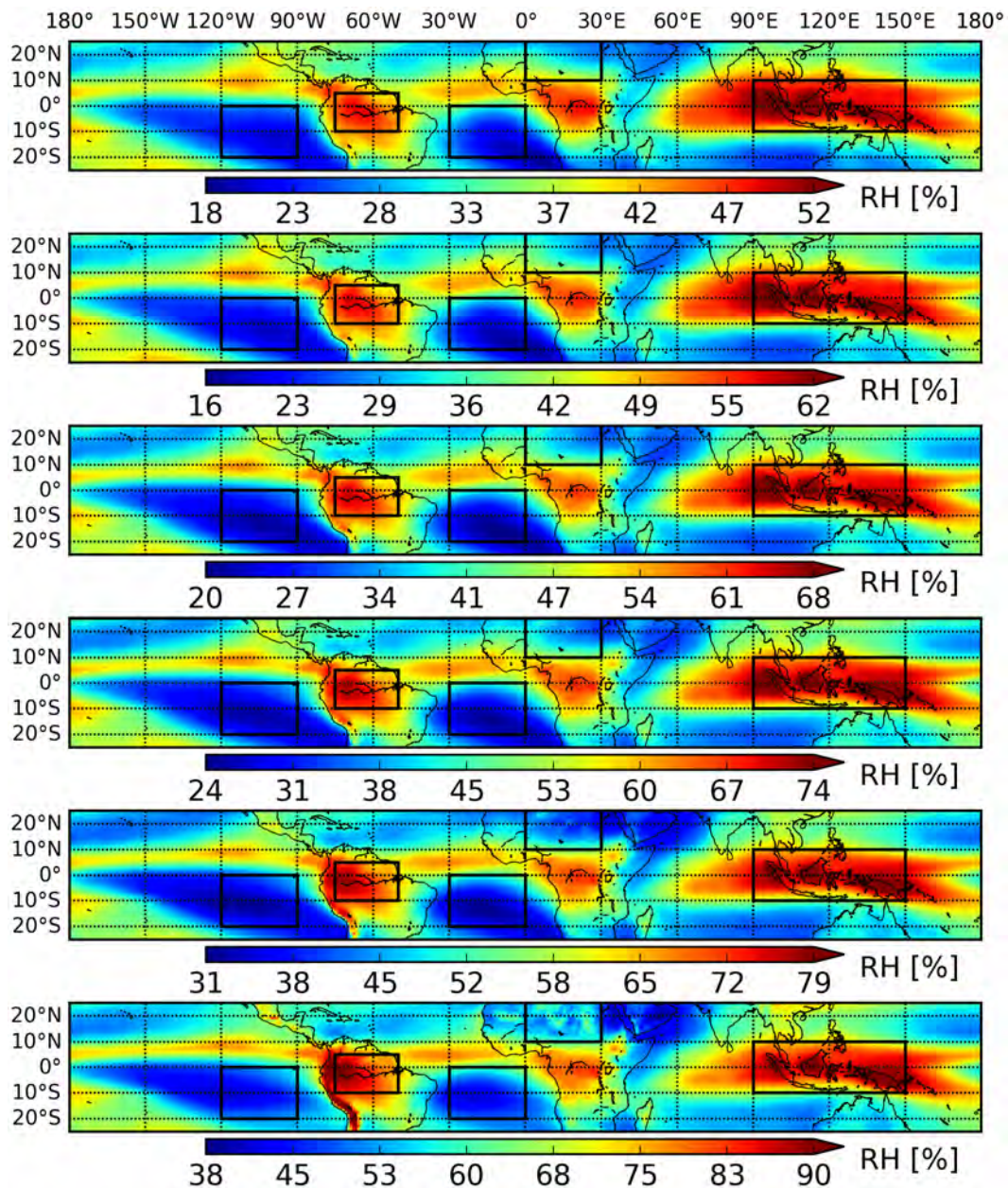


Figure 7. Spatial distribution of layer-averaged RH_I derived using SAPHIR data for the period January 2012 to September 2015. Depicts from top to bottom are for SAPHIR channels 1-6, respectively.

290 ously depend on the satellite overpass time (see Section 4.3 for more details). The same figures are included in the supplementary materials for the error in RH_L .

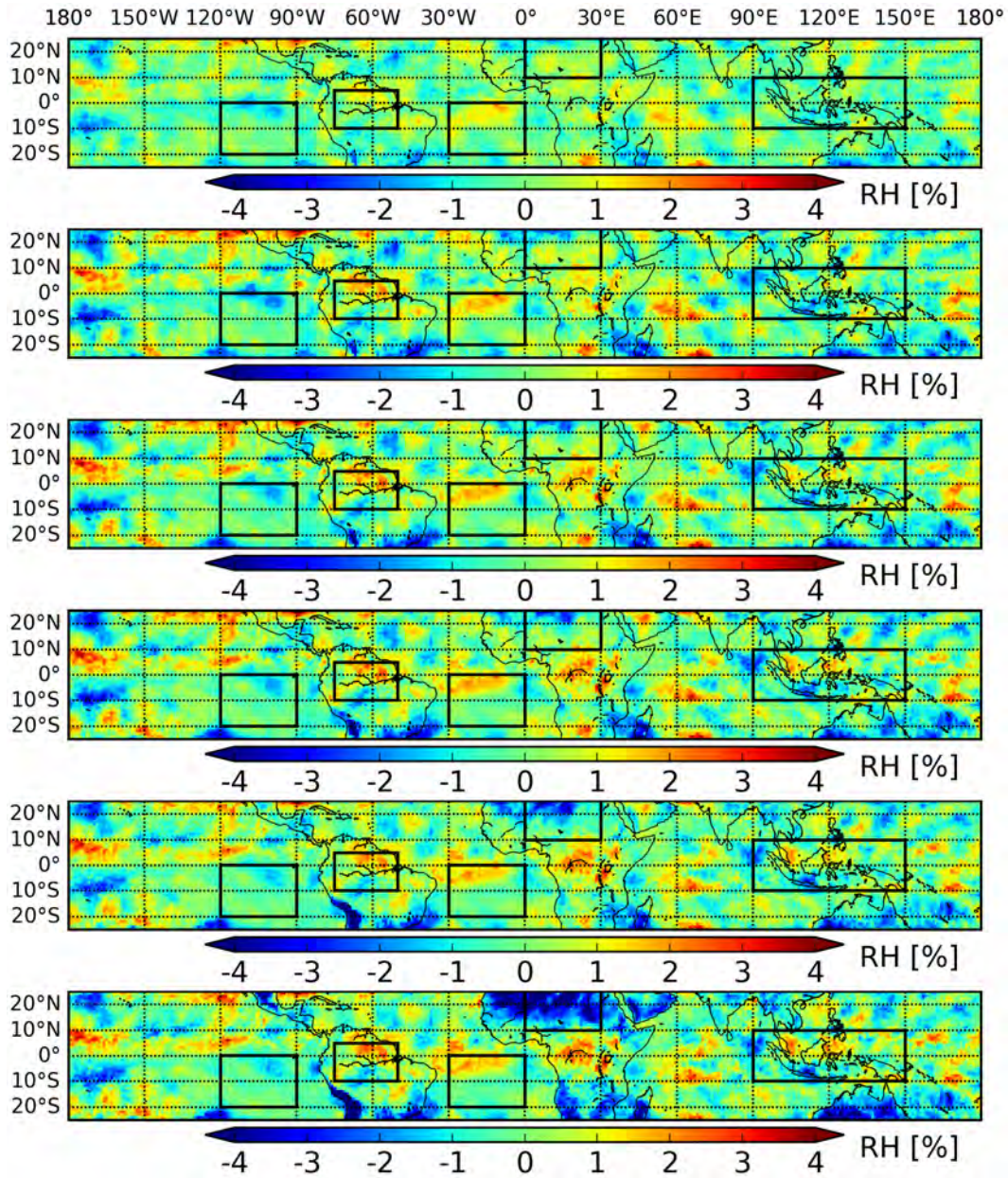


Figure 8. Mean difference of daily average of RH_I calculated using only data from 01:30/13:30 local time and the daily average calculated using all hourly data. Depicts from top to bottom are for SAPHIR channels 1-6, respectively.

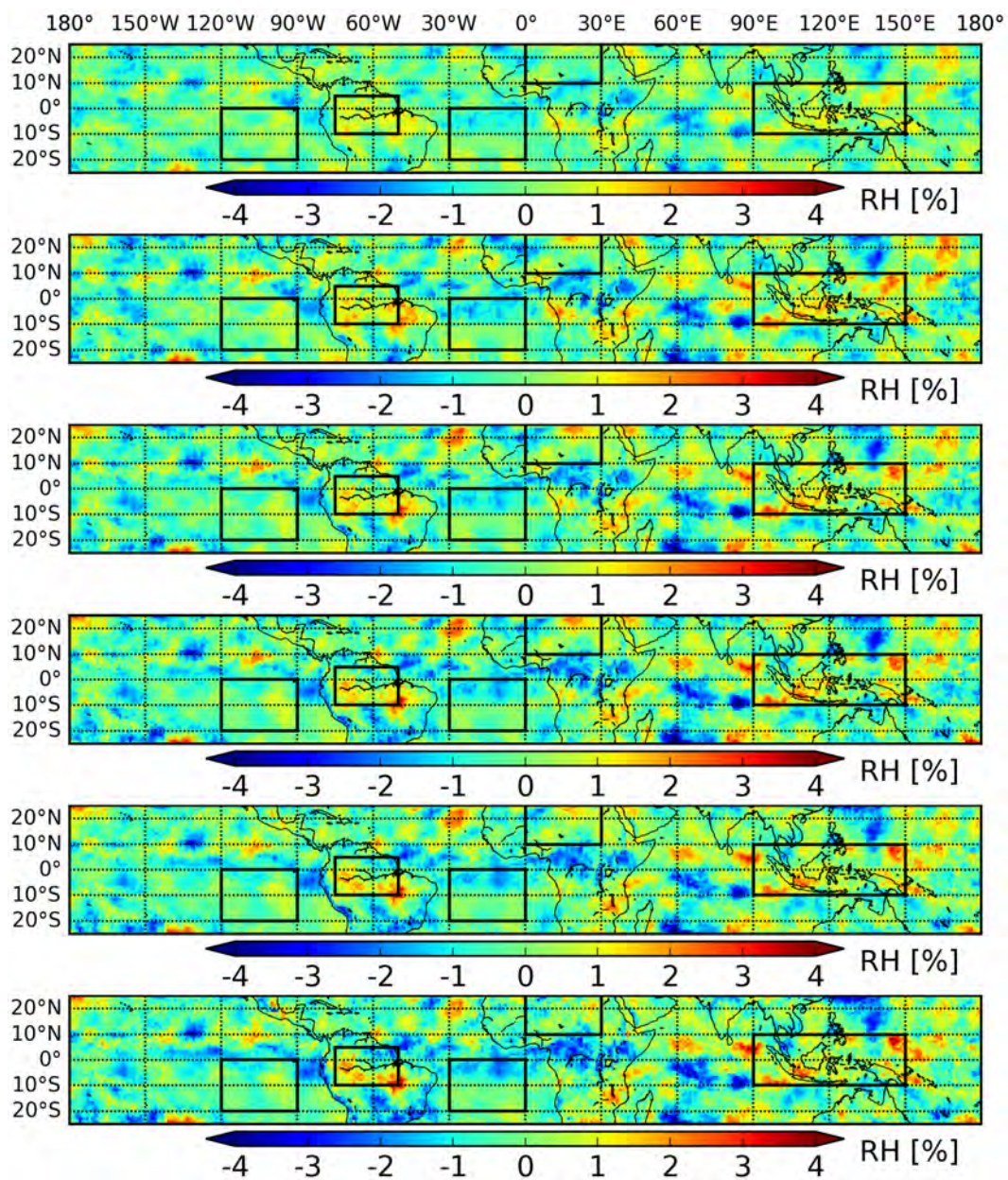


Figure 9. Mean difference of daily average of RH_I calculated using only data from 09:30/21:30 local time and the daily average calculated using all hourly data. Depicts from top to bottom are for SAPHIR channels 1-6, respectively.

4.3 Amplitude and Peak Time

Figure 10 shows the diurnal amplitude of layer-averaged RH_I as the difference between maximums and minimums of RH derived from the Fourier series fit over the course of the day. We employ the diurnal amplitude and peak time derived from the Fourier series, because they are more stable and less noisy than the amplitude and peak time derived from the measurements, though both Fourier series and measurements yield very similar results. The diurnal amplitude derived from the measurements is included in the supplementary materials. The pattern and magnitude of the amplitude significantly change from upper to lower troposphere. In upper and middle troposphere, i.e., Channels 1-4, the diurnal amplitude is less than 15 % with the maximum occurring over the Andes, South Africa, Madagascar, and Australia as well as some scattered places over South America and Arabian Desert. The diurnal amplitude in upper troposphere is consistent with Eriksson et al. (2010) who reported up to 8 % change over tropical land regions in upper troposphere. However, in lower troposphere, the amplitude can be up to 29 % over land. In lower troposphere, the diurnal amplitude is generally less than 10 % over ocean, but over deserts and mountains the amplitude is greater than 15 % with maximum occurring over deserts of South and North Africa, Australia, Middle East, the Andes in South America, and the Sierra Madres mountains in Mexico. The diurnal amplitude for RH_L (see the supplementary materials) is a few percent smaller than that for RH_I but the pattern is very similar. The amplitude slightly changes from channel 1 to channel 5, but it is much larger for channel 6 than for channel 5 (29 % versus 19 % over land). However, the pattern is very similar for channels 5 and 6. Generally, a stronger diurnal amplitude is found over land than over ocean for the lower channels. This can be explained by the fact that the diurnal variation of RH in the lower layers of the troposphere is enforced by the change in surface and boundary layer temperature which are larger over land than over ocean. Over ocean, the diurnal amplitude tends to be larger over convective regions than over subsidence regions which is consistent with previous studies (e.g., Chung et al., 2007).

Since the location of ITCZ changes with time, the diurnal amplitude and peak time are expected to be seasonal dependent. The ITCZ location is furthest away from the equator during Summer Solstice (towards north) and Winter Solstice (towards south), therefore, in addition to examining the annual averages of the diurnal amplitude and peak time, we separately evaluated the diurnal amplitude and peak time for the months of December and January (Winter Solstice, Figure 11) as well as June and July (Summer Solstice, Figure 12). Comparing the diurnal amplitude of RH derived from the annual averages (Figure 10) with Figures 12 and 11 shows that the change in diurnal amplitude during Summer Solstice is larger than the change during the Winter Solstice. This is because due to the presence of more continents in the northern hemisphere, ITCZ moves further away from the equator during Summer Solstice (Waliser and Gautier, 1993). The main difference between the diurnal amplitudes of Winter and Summer Solstices can be summarized as follows. The amplitudes in all layers are about 2 % higher in Winter Solstice than in the Summer Solstice. Shift

in ITCZ forces the convective region over Central Africa to move to the southern latitudes during
330 Winter Solstice. Therefore, North Africa is dominated by a dry subsidence region during Winter
Solstice which causes a larger diurnal amplitude especially in the lower troposphere likely due to a
larger diurnal cycle in air temperature. In contrast, in summer Solstice, ITCZ moves to the northern
latitudes so that most African continent is dominated by a convective region, except South Africa,
which causes a smaller diurnal amplitude during Summer Solstice. In addition, the diurnal amplitude
335 over North America is considerably lower during Summer Solstice than the Winter Solstice.

Figure 13 shows the RH_I diurnal peak time for different channels derived from the Fourier series
fit. The peak time derived from the measurements is shown in the supplementary materials. Gen-
erally, over most regions, the peak time is delayed from upper to lower troposphere. For instance,
over Africa the diurnal peak time changes from midnight in the upper troposphere to early morning
340 in the lower troposphere. Overall, the peak-time occurs around mid-night over most continental
regions which is consistent with previous studies (e.g., Chung et al., 2007). Over oceans, the peak-
time normally happens in the morning over subsidence regions but mid-night over the convective
regions. It should be noted that there is a large uncertainty in estimating the peak time when the
diurnal amplitude is very small. Generally, the early morning peak time that has been reported be-
345 fore (e.g., Soden, 2000; Tian, 2004; Chung et al., 2007; Eriksson et al., 2010; Kottayil et al., 2013),
only occurs in some regions and it is not common for the entire tropical region. The early morning
peak time is due to a peak in deep convective activities (Haffke and Magnusdottir, 2015; Albright
et al., 1985). In upper troposphere, the nighttime peak time over land is generally consistent with
Chung et al. (2007), however Chung et al. (2007) reported a late-afternoon/evening peak time over
350 the convective regions which is not consistent with the current study. This can be due to the fact that
the peaktime derived from IR data is affected by the cloud screening method. Channel 3 in Kottayil
et al. (2013) (middle panel in Figure 5) can be directly compared with channel 2 in this study. Over
South America (Amazonian region) both studies show night-time peak time. However, over some
other regions, e.g., Indian Ocean, the results are not consistent. We show a peak time before 00:00 LT
355 over most part of Indian Ocean but Kottayil et al. (2013) reported a night-time peak (between 00:00
and 02:00 LT). We have filtered cloud contaminated data, therefore the results are not dominated by
cloud diurnal regime in the tropical region. Since Kottayil et al. (2013) did not exclude the surface
affected data, the results for the lower channels cannot be compared.

Haffke and Magnusdottir (2015) reported a large inhomogeneity in the diurnal variation of precip-
360 itation which is consistent with the inhomogeneity we have found for relative humidity. Using Trop-
ical Rainfall Measuring Mission (TRMM) Precipitation Radar measurements, Biasutti et al. (2011)
reported a large difference between diurnal variation of precipitation over coastal lands (early after-
noon peak) and near shores (early morning) influenced by the land/sea breeze. These fine structures
cannot be detected in MW observations due to coarse spatial resolution, but it highlights the fact
365 that the results over inhomogeneous regions such as coastal regions may not be very representative.

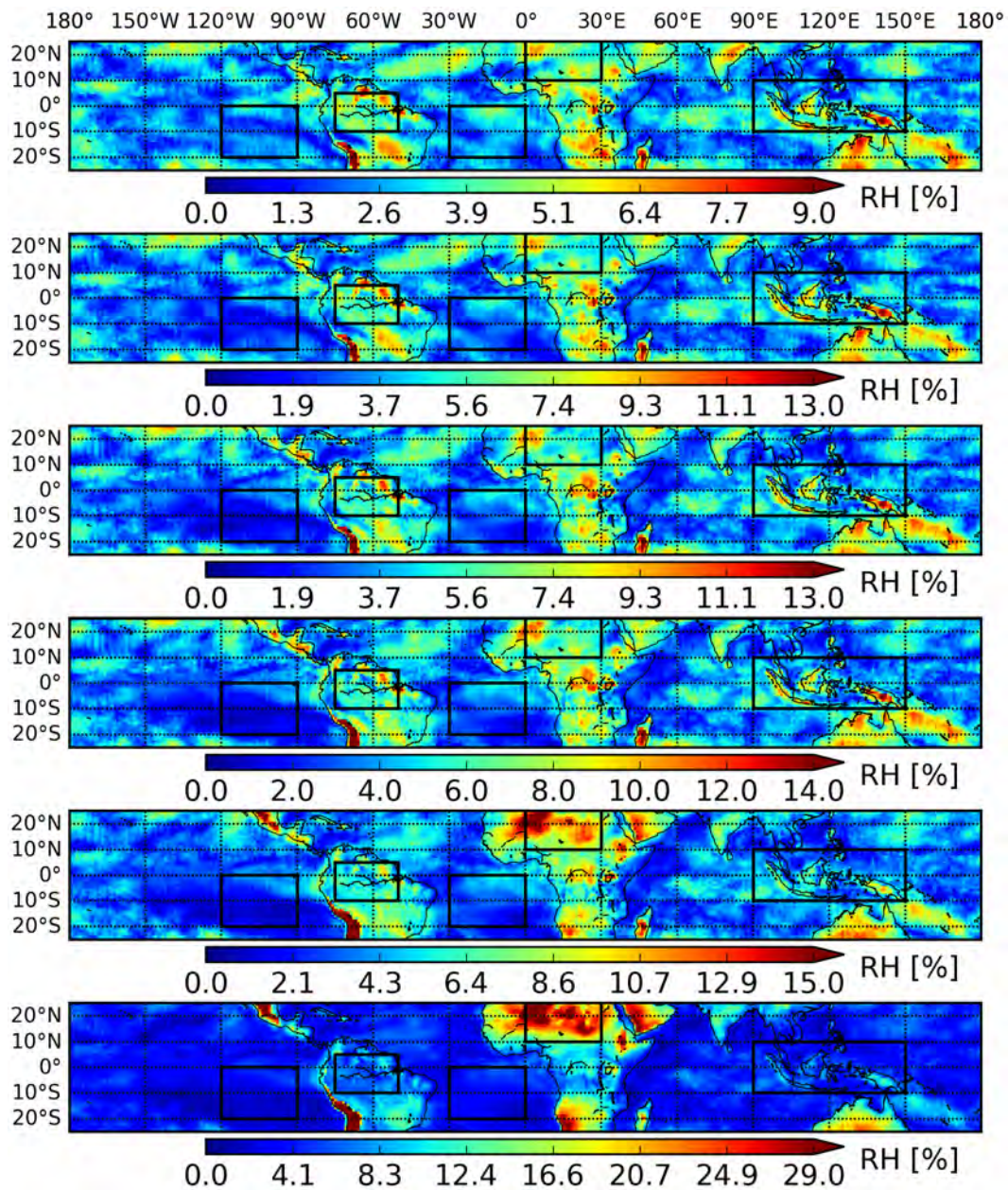


Figure 10. Spatial distribution of diurnal amplitude of RH_I . Depicts from top to bottom are for SAPHIR channels 1-6, respectively.

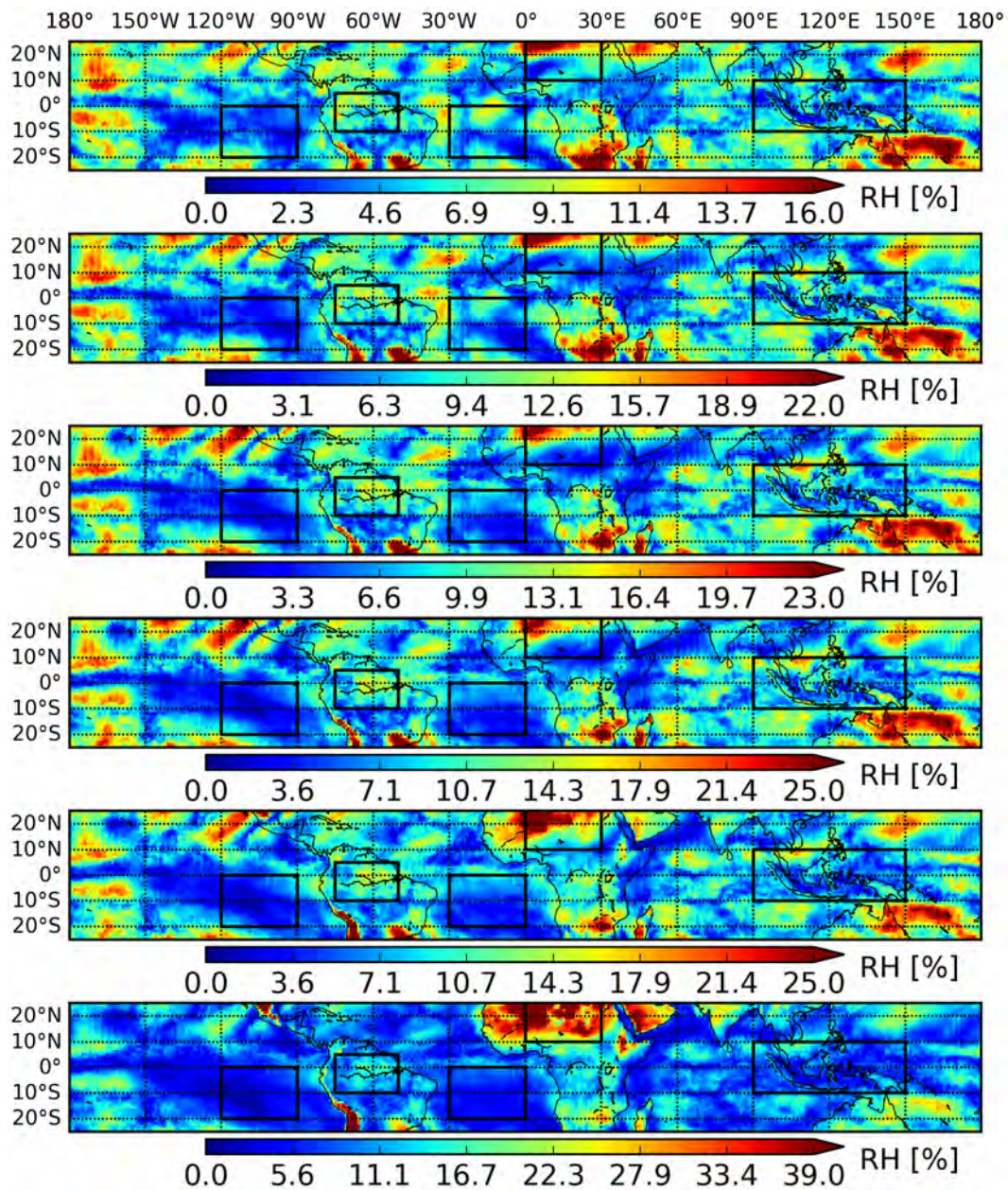


Figure 11. Spatial distribution of diurnal amplitude of RH_7 for the months of December and January. Depicts from top to bottom are for SAPHIR channels 1-6, respectively.

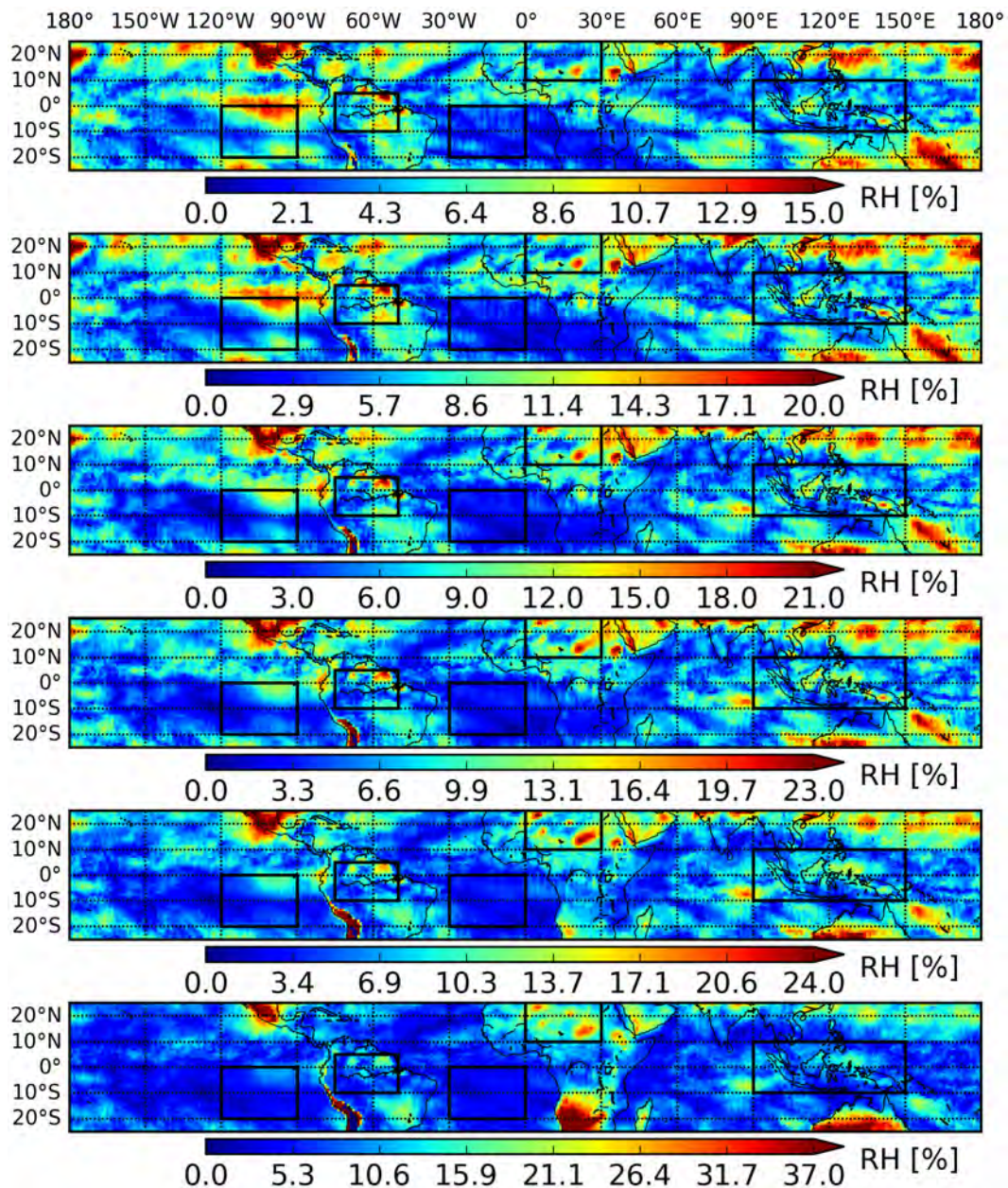


Figure 12. Spatial distribution of diurnal amplitude of RH_7 for the months of June and July. Depicts from top to bottom are for SAPHIR channels 1-6, respectively.

Although, the spatial resolution of the SAPHIR observations do not provide a sharp transition from ocean to land, a distinct peak time is observed along some of the shorelines. For instance, on the west coast of South America, the peak time over lands near shore occurs a few hours earlier than the peak time for both inland and free waters.

370 Figures 14 and 15 shows the peak-time for Winter and Summer Solstices respectively. The most distinguishable difference between the peak-times during Winter and Summer Solstices are as follows. Over Eastern Pacific, in the middle and lower troposphere, the peak mostly happens in the early morning during Summer Solstice but late evening and midnight during Winter Solstice. A nighttime peak is observed over Africa during Summer Solstice but the peak-time changes to early morning
 375 during Winter Solstice. Over Indian Ocean, there is an early morning peak-time during Summer Solstice that changes to a late-evening and midnight peak during Winter Solstice.

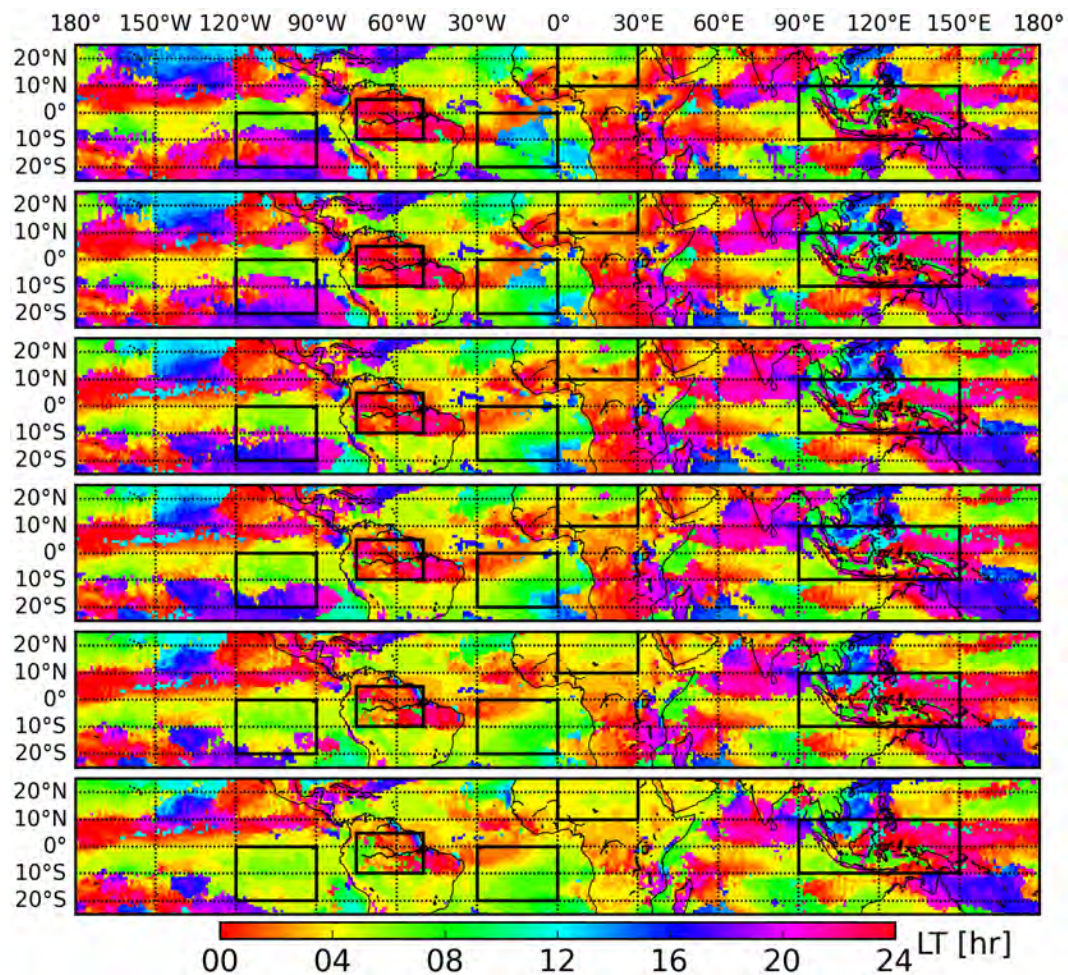


Figure 13. Diurnal peak time in local time for RH_1 based on Fourier series fit. Depicts from top to bottom are for SAPHIR channels 1-6, respectively.

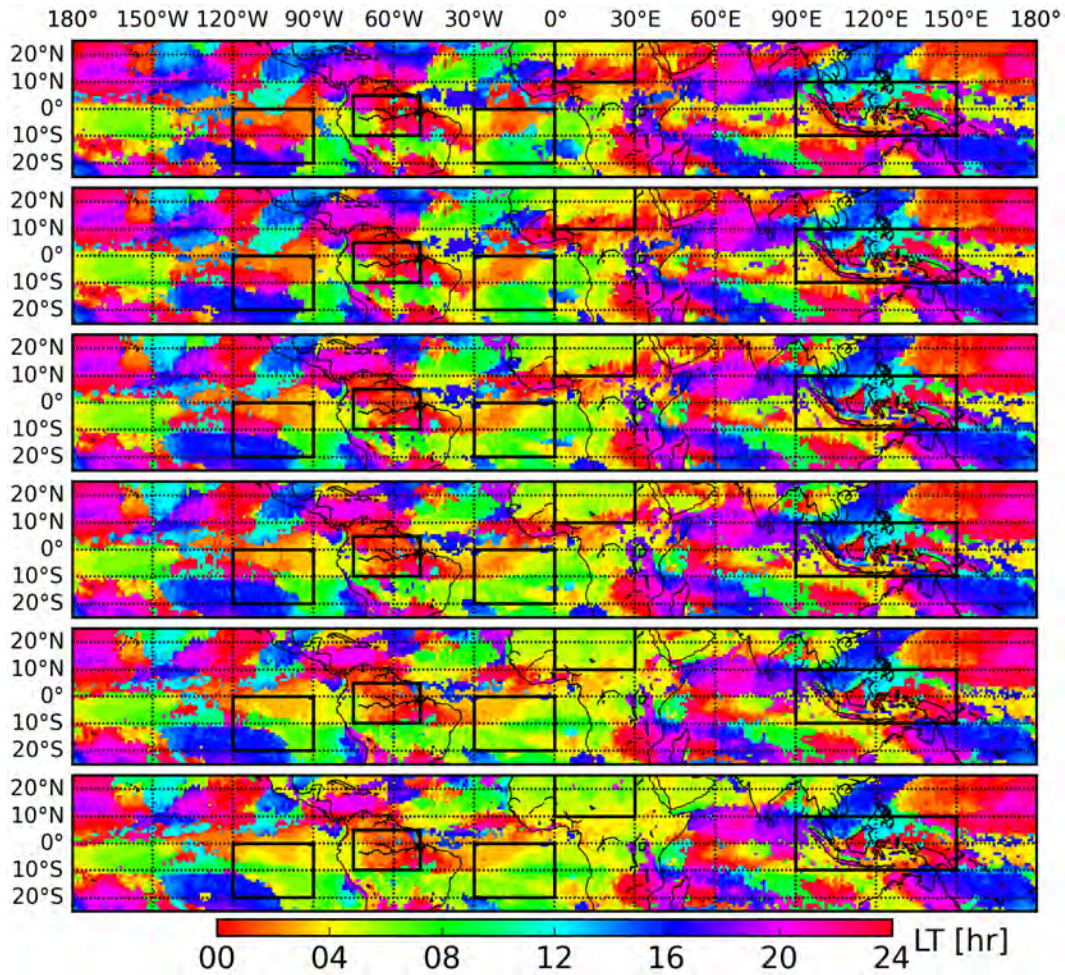


Figure 14. Diurnal peak time in local time for RH_I based on Fourier series fit for the months of December and January. Depicts from top to bottom are for SAPHIR channels 1-6, respectively.

Based on the mean and diurnal amplitude of RH, five regions are selected that will be used to further investigate some of the results. The coordinates (minimum and maximum of latitudes and longitudes) of these rectangular regions are shown in Table 2. These regions from west to east are located over South Pacific Ocean, Amazon, South Atlantic Ocean, North Africa, and the Maritime
 380 Continent. These regions are selected in a way to present a high diversity in diurnal amplitude as well as mean tropospheric RH. The boundaries for these regions are shown on all the maps.

4.4 Diurnal Cycle of RH

The diurnal cycle of tropospheric RH is modeled using Fourier series and the series themselves can
 385 be demonstrated using the Fourier coefficients. As mentioned before, Fourier series can be theoretically expanded by infinite terms but in practice only a few terms are required for diurnal variation of

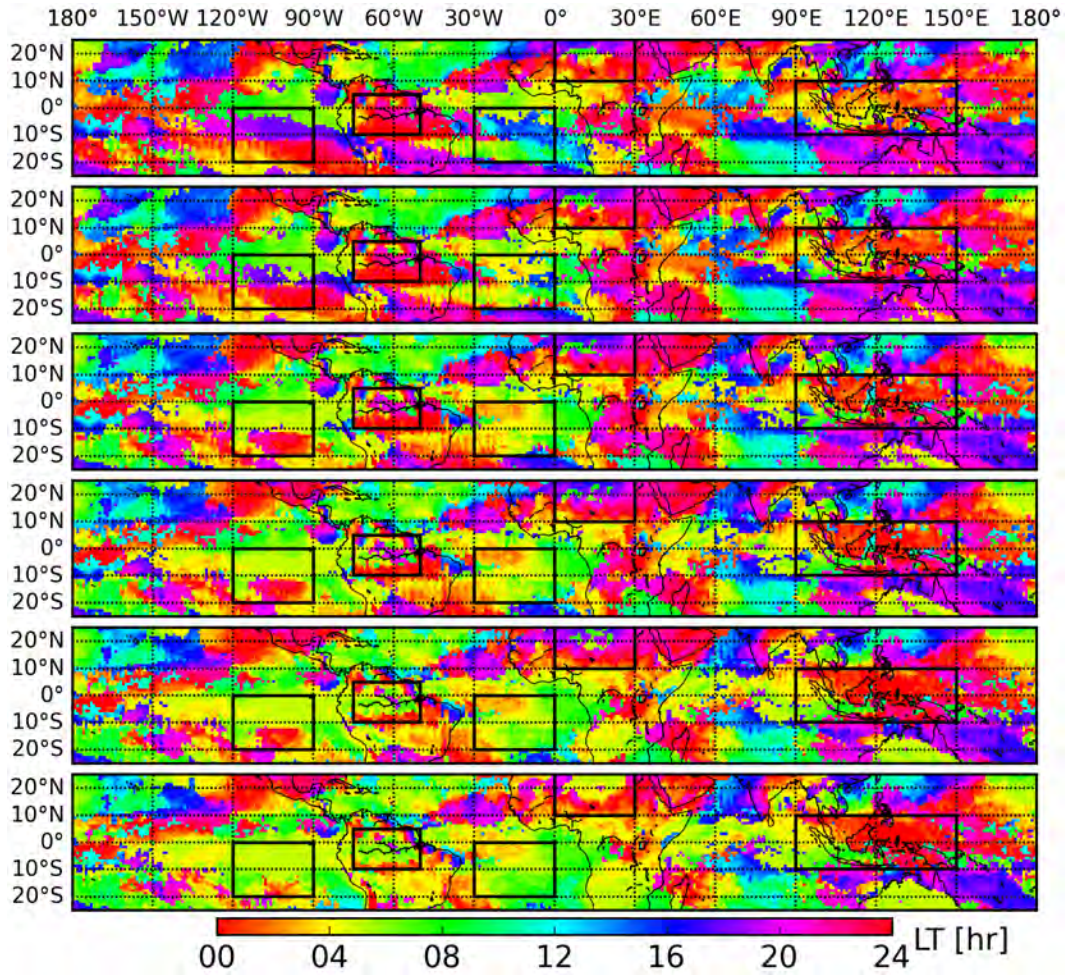


Figure 15. Diurnal peak time in local time for RH_I based on Fourier series fit for the months of June and July. Depicts from top to bottom are for SAPHIR channels 1-6, respectively.

Table 2. The regions selected based on mean and amplitude of tropospheric RH to investigate the diurnal variation of RH. The regions are labeled from west to east as South Pacific Ocean (SP), Amazon (AM), South Atlantic Ocean (SA), North Africa (NA), the Maritime Continent (MC), and entire Tropical Region (TR). These regions are indicated on all the maps.

Label	Lat1	Lat2	Lon1	Lon2
SP	-20	0	-120	-90
AM	-10	5	-75	-50
SA	-20	0	-30	0
NA	10	25	0	30
MC	-10	10	90	150
TR	-25	25	-180	180

meteorological variables. In this study, we expanded the Fourier series in only two terms, i.e., $k=1,2$. As mentioned earlier, this number was determined by analyzing the difference between the measurements and the values estimated using Fourier series. For instance, Figure 16 shows the mean absolute difference between the measurements and the Fourier series fit. Over most regions the difference is less than one percent when the series are expanded in two terms.

Since the coefficient a_0 is equal to the mean of the measurements, its distribution is already shown in Figures 6 and 7. The coefficient a_k and b_k present information about the phase and amplitude of the signal and are included in the supplementary materials. If we rewrite the Fourier coefficients as a complex number $z_n = a_n + ib_n$ then the amplitude and phase can be expressed using $|z|$ and $arg(z)$:

$$|z| = \sqrt{zz^*} = \sqrt{a^2 + b^2} \quad (5)$$

$$arg(z) = x = \tan^{-1}\left(\frac{b}{a}\right) \quad (6)$$

where, $arg(z)$ is the phase difference ranging from $-\pi$ to π and can be converted back to the time of the day using $t = (12x/\pi) + 12$.

In the following, the selected regions will be used to further investigate the diurnal variation of tropospheric RH using Fourier series. Figure 17 shows the diurnal cycle of the layer-averaged RH_I (absolute values) in selected regions for different SAPHIR channels. Figure 18 shows the RH values scaled between -100 and 100 to better distinguish the diurnal cycle for regions with a small diurnal amplitude. As shown, in most regions the diurnal amplitude is very small (less than a few percent), but the diurnal amplitude in middle and lower troposphere over North Africa is greater than 10 % (consistent with Figure 10). In upper troposphere (Channels 1 and 2), the diurnal variation is less than 5 % over all selected regions. As shown in Figure 18, some regions such as SP and SA experience two peaks. Over SP, one of the peaks happens in early morning and other one in the evening. The evening peak is stronger in upper troposphere, but in lower troposphere the morning peak becomes stronger than the evening peak. A similar pattern exist over SA, however the second peak occurs around early afternoon and becomes weaker from upper to lower troposphere. However in both cases the actual amplitude of the diurnal cycle is a very small percentage. The double peak is consistent with a double peak in precipitation reported in Dai (2001). Note that peak in precipitation normally coincide with a minimum in RH. As reported in Chung et al. (2007) the RH trend, at least in upper troposphere, follows the trend in convective clouds except the minimum of RH that occurs when the precipitation starts to increase. As shown in Figure 17, the peak time slightly shifts from upper to lower troposphere. The amplitude over North Africa also changes significantly from a few percent in upper troposphere to more than 20 % in lower troposphere which is due to change in the diurnal variation of air temperature. Figure 17 also includes an example for a grix-box with a large difference between the measurements and the fit for the Fourier series. The grid-box is located near Lago Salar de Arizaro (24.5° S, 67.5° W), a small salt flat of the Andes in Argentina. The surface area of the flat

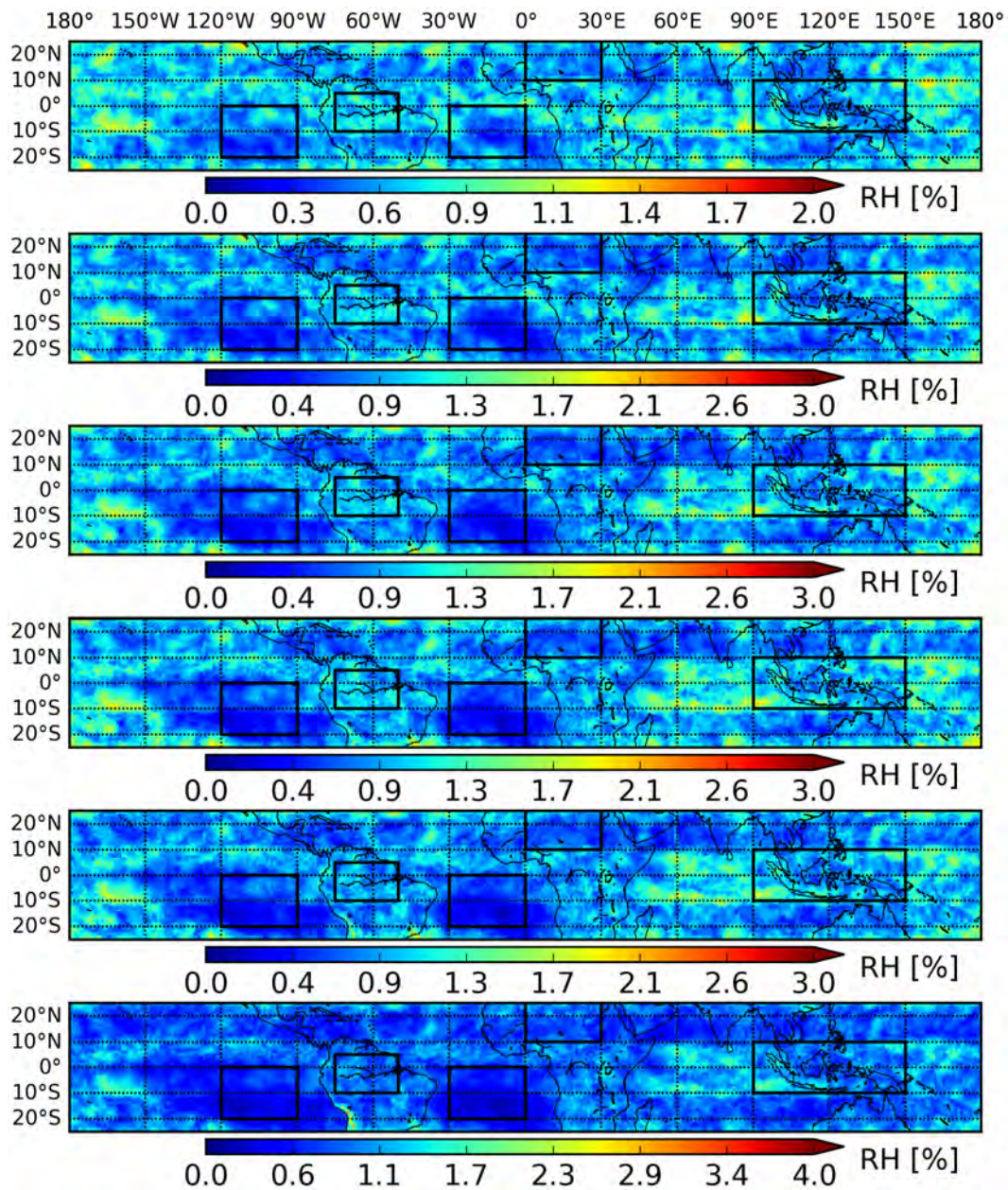


Figure 16. Mean absolute difference (with respect to ice) between measurements and the fit for Fourier series. Depicts from top to bottom are for SAPHIR channels 1-6, respectively.

is only 1600 km², therefore the grid-box covers a mix of the salt flat and the surrounding terrains. As shown, the Fourier series are perfectly fitted to the data and the difference between the measurements and the Fourier series fit is rather due to noise in the data.

425 4.5 Distribution Functions

Figure 19 shows the distribution of layer averaged RH with respect to both liquid and ice over selected regions. In addition, the cumulative distribution functions are also provided in the supplementary materials. As shown the distributions of RH with respect to ice and water are similar in the lower troposphere (channels 5 and 6). This is because the relative humidity values calculated using
430 Equation 1 are nearly the same over ice and liquid for the expected range of brightness temperatures in lower troposphere. This is an indication that the transition from ice to liquid is performed smoothly. When necessary, we use RH over ice for channels 1-4, and over water for channels 5-6 to discuss the results. Overall, the distribution functions are very similar for the Amazon and the Maritime Continent regions. Some small differences exist between the two regions especially in the
435 upper troposphere, where the Maritime Continent tend to be more moist than Amazon. The distribution functions are also similar for South Pacific and South Atlantic, but South Atlantic tends to be slightly more moist than South Pacific in all layers. Therefore, we only explain distribution functions for South Atlantic, the Maritime Continent, and North Africa in more detail. The first and third quartiles of the distribution functions are used to explain the range of RH in each layer. The range of
440 RH between first and second quartile include 50% of the data-points. For channel 1, the first (third) quartiles are 15(25), 40 (55), 20 (40), over South Atlantic, the Maritime Continent, and North Africa. None of the regions show a normal distribution function. The distribution is left-skewed (the left tail is longer) for Amazon and the Maritime Continent, and right-skewed over the rest of the selected regions. The shape of the distribution remains almost similar for other channels. The quartiles are
445 very similar between channels 1 and 2, but increase about 5% per layer for channels 3-5. So that the quartiles for each lower channel are about 5% higher than the same quantities for the channel peaking above it. From channels 5 to channel 6, the increase in quartiles is about 10%. Note that in many cases the minimum and maximum are very close to first and third quartile meaning that 25% of the datapoints lie within a small range of RH. A small percentage of the data show supersaturation
450 over liquid (up to 110 %) for Channel 6. This can be explained by the methodological error as well as error in the satellite observations. We estimate that the error introduced by difference sources (see Section 4.6) can be up to 15 %. Our findings for SAPHIR Channels 1 and 2 are generally consistent with Eriksson et al. (2010), especially for the results presented for AURA-MLS instrument. For instance both studies show that the RH_I can reach up to 80 % over Africa. However, Eriksson et al.
455 (2010) reported a maximum RH_I of 80 % to 100 % over the Maritime Continent but our results show a maximum of 60 % to 80 % for SAPHIR Channel 1 and 80 % to 100 % for SAPHIR Chan-

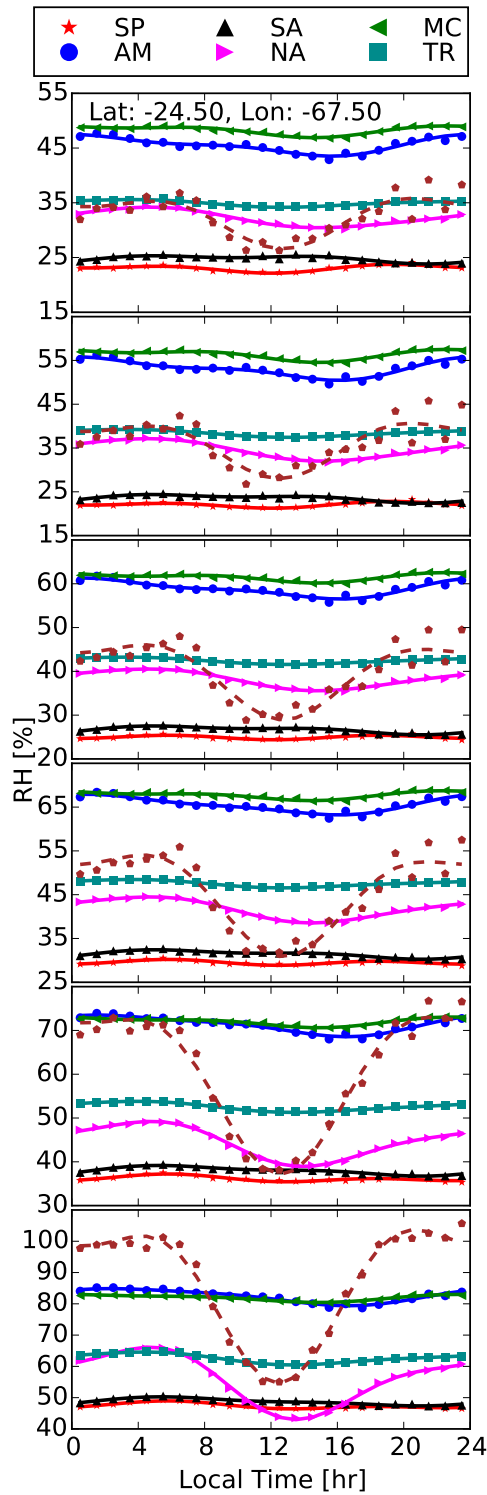


Figure 17. Diurnal cycle of layer-averaged RH_I as well as Fourier series fit for the selected regions. Depicts from top to bottom are for SAPHIR channels 1-6, respectively. The legend shows the name of the regions which are defined in Table 2. The dashed lines show a grid box with a large difference between the measurements (pentagons) and the fit for the Fourier series (the dashed-line). The longitude and latitude of this grid-box are printed on the top plot.

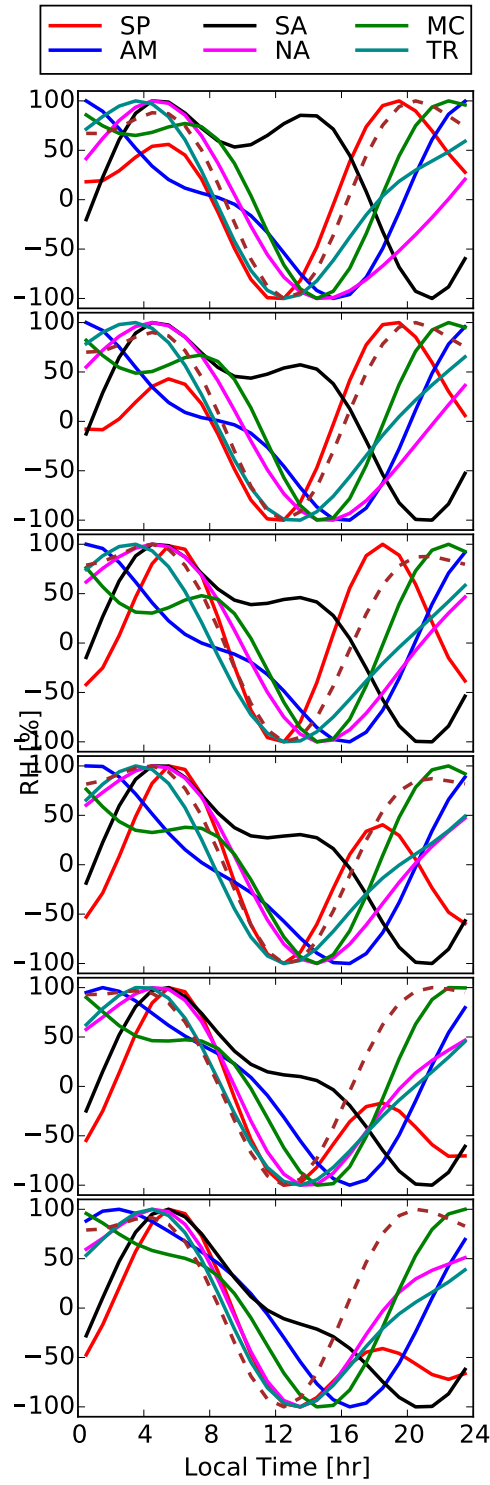


Figure 18. Same as Figure 17 but the values are scaled between -100 and 100.

nel 2. Overall, it is expected that the cloud filter removes some supersaturated regions in our study, because those regions are normally associated with the cloud formation.

4.6 Error Estimates

460 In this section, the error sources are discussed, though it is not possible to quantitatively estimate most of the errors. One obvious source of error is bias and noise in the satellite data. According to Moradi et al. (2015b) the bias in SAPHIR data should be less than 0.5 K which is roughly equal to 5 % in RH space. Although, the bias affects the RH values, it does not affect the results for diurnal amplitude and peak time. Since a large volume of the data is averaged, the noise in the satellite data
465 should cancel out if the relation between RH and T_b was linear. However, due to the non-linear relation between the two, the random noise may not completely cancel out. Another source of error is from the T_b to RH transformation method which according to Moradi et al. (2015a) is estimated to be less than 10 %. Other sources of error include the surface and cloud effects. Although we have applied appropriate filters, it is still possible that some clouds are not filtered out and at least
470 for the lower channels there are still cases that are affected by the surface. The limb-correction technique is based on satellite data averaged over the entire tropics. Therefore, it may introduce at least some noise in the correction for the individual measurements. However, it is expected that the limb-correction does not introduce a systematic bias. The random error introduced by the limb-correction technique may not completely cancel out due to the non-linear between RH and T_b .
475 However, the overall impact of the random error on the results is expected to be negligible. Finally, diurnal variation of RH is highly influenced by the diurnal variation of air temperature, thus sources such as inversion in temperature lapse rate can contribute to the error because satellite data are averaged over a wide layer.

5 Conclusions and Summary

480 Water vapor significantly influences the Earth's climate because of its greenhouse effect. Water vapor is also important to the global water and energy budget. Free tropospheric water vapor, especially in the tropical region, significantly contributes to the water vapor feedback through radiative processes (Held and Soden, 2006; Trenberth et al., 2009; Dessler and Sherwood, 2009; Dessler et al., 2008). Therefore, it plays an important role in global warming and climate change predictions (Cess
485 et al., 1990). Despite the importance of water vapor and its diurnal variation, current climate and numerical weather prediction models do not adequately simulate the diurnal variation of tropospheric humidity (Chung et al., 2013). Accurate and comprehensive observations are required to validate the simulations of these models. Most studies, so far have used IR measurements to investigate changes in tropical tropospheric RH, but because of high sensitivity of IR channels to clouds, these studies
490 are significantly biased toward analyzing dry conditions as cloud screening methods remove moist

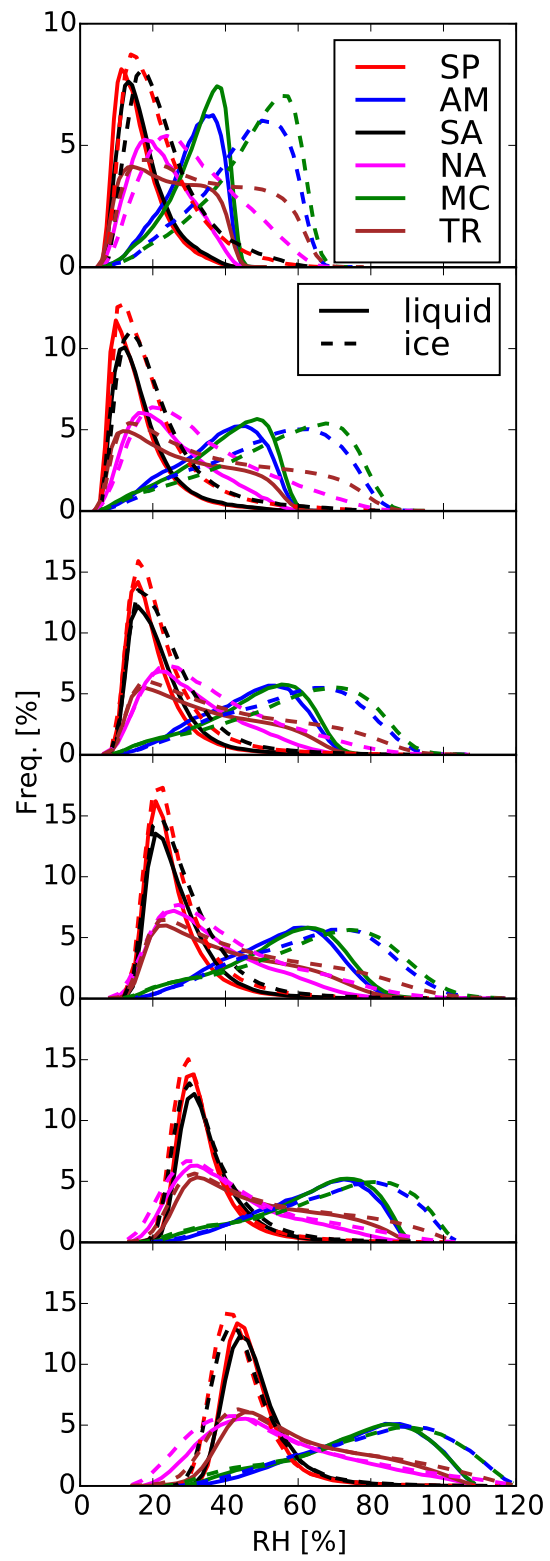


Figure 19. Distribution functions for both RH_I and RH_L . Depicts from top to bottom are for SAPHIR channels 1-6, respectively. The legend shows the name of the regions which are defined in Table 2.

regions from the analysis. Some previous studies have used multi-instrument microwave observations to study diurnal cycle of RH, but due to inter-satellite differences there is a large uncertainty in such studies. SAPHIR is a microwave instrument onboard Megha-Tropiques that provides frequent observations in the tropical region with frequent daily revisits.

495 In this study, we first transformed the satellite Tb's into layer-averaged RH, then binned the SAPHIR data using the location and local observation time into a grid of $1.0^\circ \times 1.0^\circ \times 1.0$ hr. Finally, we fitted the Fourier series to the data within each grid-box. The daily-averaged RH values showed that the moist regions are associated with the convective regions and the dry regions are associated with the subsidence regions. The results showed an early morning peak time for most tropical
500 band, but there are several regions where the peak time occurs over night or in the afternoon. The amplitude significantly changes from upper to lower troposphere especially over lands. So that the maximum amplitude is less than 10 % in upper troposphere but up to 29 % in lower troposphere. The results were analyzed separately for RH with respect to saturated vapor pressure over both ice and liquid. The results for both phases are either included in the paper or in the supplementary materi-
505 als. The analysis shows that microwave measurements from low-inclination satellites are a valuable source for investigating the diurnal and spatial variation of tropospheric RH. The application of the current data is limited to RH as these measurements are most sensitive to the RH than absolute humidity parameters such as specific humidity. The microwave temperature imaging instrument on the same satellite failed shortly after the satellite was launched, otherwise it would have been possible
510 to perform the same analysis for the tropical tropospheric temperature.

Appendix A: Fourier Series

Fourier coefficients for any known function can be calculated using the following relations:

$$\begin{aligned}
 a_0 &= \frac{1}{2\pi} \int_{-\pi}^{\pi} f(x) dx \\
 a_k &= \frac{1}{\pi} \int_{-\pi}^{\pi} f(x) \cos(kx) dx \\
 515 \quad b_k &= \frac{1}{\pi} \int_{-\pi}^{\pi} f(x) \sin(kx) dx
 \end{aligned} \tag{A1}$$

The relations presented in Equation A1 are useful when the Fourier series are used to approximate a known function but in our specific case, $f(x)$ is unknown and need to be approximated. These relations can be discretized based on a Riemann sum and the measurements of RH as follows:

$$\begin{aligned}
a_0 &= \frac{1}{2\pi} \sum_{i=1}^n y_i \Delta x = \frac{1}{n} \sum_{i=1}^n y_i = \bar{y} \\
520 \quad a_k &= \frac{1}{\pi} \sum_{i=1}^n y_i \cos(kx_i) \Delta x = \frac{2}{n} \sum_{i=1}^n y_i \cos(kx_i) \\
b_k &= \frac{1}{\pi} \sum_{i=1}^n y_i \sin(kx_i) \Delta x = \frac{2}{n} \sum_{i=1}^n y_i \sin(kx_i)
\end{aligned} \tag{A2}$$

In case, different weights are given to the measurements then Equation A1 can be rewritten as shown in Equation 4.

Acknowledgements. This study was supported by NOAA grant# NA09NES4400006 (Cooperative Institute for
525 Climate and Satellites - CICS) at the University of Maryland, Earth System Science Interdisciplinary Center (ESSIC). Part of the research was carried out at the Jet Propulsion Laboratory, California Institute of Technology, under a contract with the National Aeronautics and Space Administration. SAPHIR data are processed and provided by Centre National d'Etudes Spatiales (CNES), France. The views, opinions, and findings contained in this report are those of the authors and should not be construed as an official National Oceanic and Atmospheric
530 Administration or U.S. Government position, policy, or decision.

References

- Albright, M. D., Recker, E. E., Reed, R. J., and Dang, R.: The diurnal variation of deep convection and inferred precipitation in the central tropical pacific during january – february 1979, *Monthly Weather Review*, 113, 1663–1680, doi:10.1175/1520-0493(1985)113<1663:TDVODC>2.0.CO;2, 1985.
- 535 Biasutti, M., Yuter, S. E., Burleyson, C. D., and Sobel, A. H.: Very high resolution rainfall patterns measured by TRMM precipitation radar: seasonal and diurnal cycles, *Climate Dynamics*, 39, 239–258, doi:10.1007/s00382-011-1146-6, 2011.
- Buehler, S. A. and John, V. O.: A simple method to relate microwave radiances to upper tropospheric humidity, *Journal of Geophysical Research: Atmospheres*, 110, D02 110, doi:10.1029/2004JD005111, 00053, 2005.
- 540 Cess, R. D., Potter, G. L., Blanchet, J. P., Boer, G. J., Del Genio, A. D., Déqué, M., Dymnikov, V., Galin, V., Gates, W. L., Ghan, S. J., Kiehl, J. T., Lacis, A. A., Le Treut, H., Li, Z.-X., Liang, X.-Z., McAvaney, B. J., Meleshko, V. P., Mitchell, J. F. B., Morcrette, J.-J., Randall, D. A., Rikus, L., Roeckner, E., Royer, J. F., Schlese, U., Sheinin, D. A., Slingo, A., Sokolov, A. P., Taylor, K. E., Washington, W. M., Wetherald, R. T., Yagai, I., and Zhang, M.-H.: Intercomparison and interpretation of climate feedback processes in 19
- 545 atmospheric general circulation models, *Journal of Geophysical Research: Atmospheres*, 95, 16 601–16 615, doi:10.1029/JD095iD10p16601, 00776, 1990.
- Chevallier, F., Di Michele, S., and McNally, A. P.: Diverse profile datasets from the ECMWF 91-level short-range forecasts, Tech. rep., NWP SAF Satellite Application Facility for Numerical Weather Prediction, 2006.
- Chung, E. S., Sohn, B. J., Schmetz, J., and Koenig, M.: Diurnal variation of upper tropospheric humidity and its
- 550 relations to convective activities over tropical africa, *Atmos. Chem. Phys.*, 7, 2489–2502, doi:10.5194/acp-7-2489-2007, 00022, 2007.
- Chung, E.-S., Soden, B. J., Sohn, B. J., and Schmetz, J.: An assessment of the diurnal variation of upper tropospheric humidity in reanalysis data sets, *Journal of Geophysical Research: Atmospheres*, 118, 3425–3430, doi:10.1002/jgrd.50345, cited by 0000, 2013.
- 555 Dai, A.: Global precipitation and thunderstorm frequencies. part II: diurnal variations, *Journal of Climate*, 14, 1112–1128, 2001.
- Dessler, A. E. and Sherwood, S. C.: ATMOSPHERIC SCIENCEa matter of humidity, *Science*, 323, 1020–1021, doi:10.1126/science.1171264, 00000 WOS:000263478400028, 2009.
- Dessler, A. E., Zhang, Z., and Yang, P.: Water-vapor climate feedback inferred from climate fluctuations,
- 560 2003–2008, *Geophysical Research Letters*, 35, L20 704, doi:10.1029/2008GL035333, 00123, 2008.
- Eriksson, P., Rydberg, B., Johnston, M., Murtagh, D. P., Struthers, H., Ferrachat, S., and Lohmann, U.: Diurnal variations of humidity and ice water content in the tropical upper troposphere, *Atmos. Chem. Phys.*, 10, 11 519–11 533, doi:10.5194/acp-10-11519-2010, 00015, 2010.
- Eriksson, P., Rydberg, B., Sagawa, H., Johnston, M. S., and Kasai, Y.: Overview and sample applications of
- 565 SMILES and Odin-SMR retrievals of upper tropospheric humidity and cloud ice mass, *Atmospheric Chemistry and Physics*, 14, 12 613–12 629, doi:10.5194/acp-14-12613-2014, 2014.
- Haffke, C. and Magnusdottir, G.: Diurnal cycle of the south pacific convergence zone in 30 years of satellite images, *Journal of Geophysical Research: Atmospheres*, 120, 2015JD023 436, doi:10.1002/2015JD023436, 2015.

- 570 Held, I. M. and Soden, B. J.: Robust responses of the hydrological cycle to global warming, *Journal of Climate*, 19, 5686–5699, doi:10.1175/JCLI3990.1, 2006.
- John, V. O., Holl, G., Allan, R. P., Buehler, S. A., Parker, D. E., and Soden, B. J.: Clear-sky biases in satellite infrared estimates of upper tropospheric humidity and its trends, *Journal of Geophysical Research: Atmospheres*, 116, D14 108, doi:10.1029/2010JD015355, 00034, 2011.
- 575 Keil, C., Röpnick, A., Craig, G. C., and Schumann, U.: Sensitivity of quantitative precipitation forecast to height dependent changes in humidity, *Geophysical Research Letters*, 35, L09 812, doi:10.1029/2008GL033657, 00016, 2008.
- Kottayil, A., John, V. O., and Buehler, S. A.: Correcting diurnal cycle aliasing in satellite microwave humidity sounder measurements, *Journal of Geophysical Research: Atmospheres*, 118, 101–113, 580 doi:10.1029/2012JD018545, 00004, 2013.
- Minschwaner, K. and Dessler, A. E.: Water vapor feedback in the tropical upper troposphere: model results and observations, *Journal of Climate*, 17, 1272–1282, doi:10.1175/1520-0442(2004)017<1272:WVFITT>2.0.CO;2, 2004.
- Moradi, I., Buehler, S., and John, V.: Comparing upper tropospheric humidity from microwave satellite instruments and IGRA radiosonde data, pp. 146–151, doi:10.1109/MICRORAD.2010.5559573, 00001, 2010. 585
- Moradi, I., Ferraro, R., Soden, B., Eriksson, P., and Arkin, P.: Retrieving layer- averaged tropospheric humidity from advanced technology microwave sounder water vapor channels, *IEEE Transactions on Geoscience and Remote Sensing*, 53, 6675–6688, doi:10.1109/TGRS.2015.2445832, 00000, 2015a.
- Moradi, I., Ferraro, R. R., Eriksson, P., and Weng, F.: Intercalibration and validation of observations from ATMS 590 and SAPHIR microwave sounders, *IEEE Transactions on Geoscience and Remote Sensing*, 53, 5915–5925, doi:10.1109/TGRS.2015.2427165, 00001, 2015b.
- Schröder, M., Roca, R., Picon, L., Kniffka, A., and Brogniez, H.: Climatology of free-tropospheric humidity: extension into the SEVIRI era, evaluation and exemplary analysis, *Atmospheric Chemistry and Physics*, 14, 11 129–11 148, doi:10.5194/acp-14-11129-2014, 00005, 2014.
- 595 Sherwood, S. C.: Direct versus indirect effects of tropospheric humidity changes on the hydrologic cycle, *Environmental Research Letters*, 5, 025 206, doi:10.1088/1748-9326/5/2/025206, 00005, 2010.
- Sherwood, S. C., Roca, R., Weckwerth, T. M., and Andronova, N. G.: Tropospheric water vapor, convection, and climate, *Reviews of Geophysics*, 48, RG2001, doi:10.1029/2009RG000301, 2010.
- Soden, B. J.: The diurnal cycle of convection, clouds, and water vapor in the tropical upper troposphere, *Geophysical Research Letters*, 27, 2173–2176, doi:10.1029/2000GL011436, 00114, 2000. 600
- Soden, B. J. and Bretherton, F. P.: Upper tropospheric relative humidity from the GOES 6.7 μm channel: method and climatology for July 1987, *Journal of Geophysical Research: Atmospheres*, 98, 16 669–16 688, doi:10.1029/93JD01283, 00243, 1993.
- Soden, B. J., Jackson, D. L., Ramaswamy, V., Schwarzkopf, M. D., and Huang, X. L.: The radiative signature of upper tropospheric moistening, *Science*, 310, 841–844, doi:10.1126/science.1115602, 00194 WOS:000233121800042, 2005. 605
- Tian, B.: Diurnal cycle of convection, clouds, and water vapor in the tropical upper troposphere: satellites versus a general circulation model, *Journal of Geophysical Research*, 109, doi:10.1029/2003JD004117, 00114, 2004.

- 610 Trenberth, K. E., Fasullo, J. T., and Kiehl, J.: Earth's global energy budget, *Bulletin of the American Meteorological Society*, 90, 311–323, doi:10.1175/2008BAMS2634.1, 2009.
- Udelhofen, P. M. and Hartmann, D. L.: Influence of tropical cloud systems on the relative humidity in the upper troposphere, *Journal of Geophysical Research: Atmospheres*, 100, 7423–7440, doi:10.1029/94JD02826, 00099, 1995.
- 615 Waliser, D. E. and Gautier, C.: A satellite -derived climatology of the ITCZ, *Journal of Climate*, 6, 2162–2174, doi:10.1175/1520-0442(1993)006<2162:ASDCOT>2.0.CO;2, 1993.